HHS Public Access

Author manuscript

Cell Rep. Author manuscript; available in PMC 2023 January 03.

Published in final edited form as:

Cell Rep. 2022 December 13; 41(11): 111805. doi:10.1016/j.celrep.2022.111805.

ΔNp63 drives dysplastic alveolar remodeling and restricts epithelial plasticity upon severe lung injury

Aaron I. Weiner[1,2,3], **Gan Zhao**[1,2,3], **Hanna M. Zayas**[1], **Nicolas P. Holcomb**[1], **Stephanie Adams-Tzivelekidis**[1,2,3], **Joanna Wong**[1,2,3], **Maria E. Gentile**[1,2,3], **Dyuthi Reddy**[1], **Joey Wei**[1], **Gargi Palashikar**[1,2,3], **Kwaku K. Quansah**[1,2,3], **Andrew E. Vaughan**[1,2,3,4,*]

[1]Department of Biomedical Sciences, School of Veterinary Medicine, University of Pennsylvania, Philadelphia, PA 19104, USA

[2]Institute for Regenerative Medicine, University of Pennsylvania, Philadelphia, PA 19104, USA

[3]Penn Lung Biology Institute, University of Pennsylvania, Philadelphia, PA 19104, USA

[4]Lead contact

SUMMARY

The lung exhibits a robust, multifaceted regenerative response to severe injuries such as influenza infection, during which quiescent lung-resident epithelial progenitors participate in two distinct reparative pathways: functionally beneficial regeneration via alveolar type 2 (AT2) cell proliferation and differentiation, and dysplastic tissue remodeling via intrapulmonary airway-resident basal p63^{+} progenitors. Here we show that the basal cell transcription factor ΔNp63 is required for intrapulmonary basal progenitors to participate in dysplastic alveolar remodeling following injury. We find that ΔNp63 restricts the plasticity of intrapulmonary basal progenitors by maintaining either active or repressive histone modifications at key differentiation gene loci. Following loss of ΔNp63, intrapulmonary basal progenitors are capable of either airway or alveolar differentiation depending on their surrounding environment both *in vitro* and *in vivo*. Uncovering these regulatory mechanisms of dysplastic repair and lung basal cell fate choice highlight potential therapeutic targets to promote functional alveolar regeneration following severe lung injuries.

In brief

Weiner et al. find that ΔNp63 is required for dysplastic remodeling of the distal lung after severe pulmonary injuries. Without ΔNp63, the basal-like cells responsible for this remodeling either

*Correspondence: andrewva@vet.upenn.edu.

AUTHOR CONTRIBUTIONS

A.I.W. and A.E.V. designed the experiments and wrote the manuscript. A.E.V. supervised experimental design. A.I.W., G.Z., H.M.Z., N.P.H., S.A.-T., J.W., M.E.G., G.P., D.R., J.W., and K.K.Q. performed experiments. A.I.W. acquired data and performed data analyses.

DECLARATION OF INTERESTS

The authors declare no competing interests.

SUPPLEMENTAL INFORMATION

Supplemental information can be found online at https://doi.org/10.1016/j.celrep.2022.111805.

terminally differentiate into airway cells or undergo a fate change into AT2s, thereby promoting functional regeneration of the alveolar epithelium.

Graphical Abstract

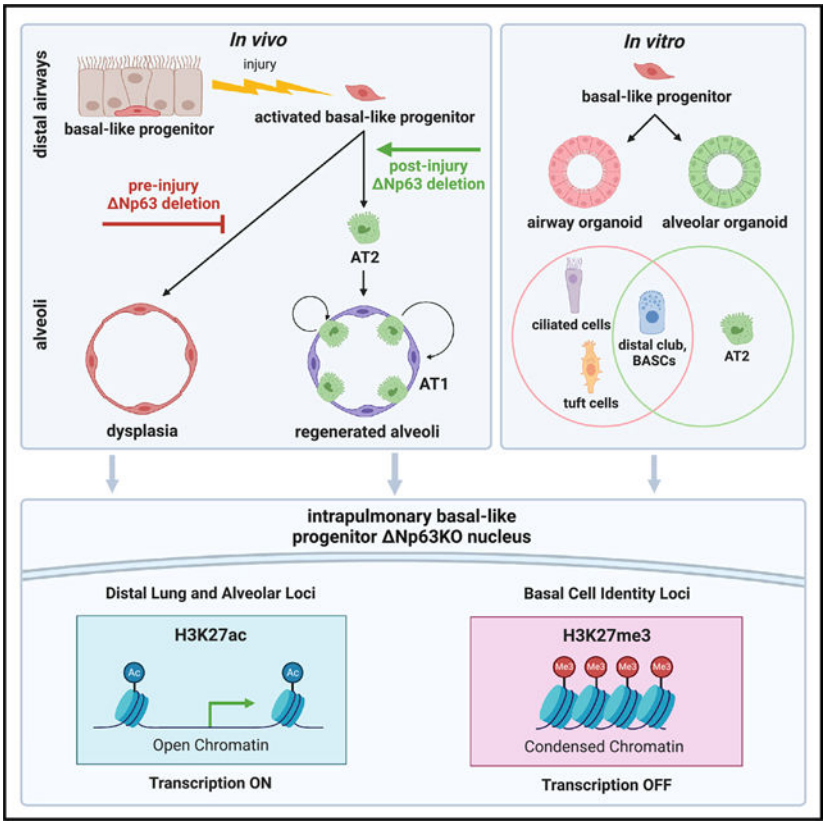

INTRODUCTION

Lung alveolar epithelial repair involves a complex interplay of multiple progenitor cell types from distinct anatomical compartments, primarily the airways and alveoli, synergizing to ultimately re-epithelialize the alveolar barrier after pulmonary injury. Severe respiratory infections and epithelial insults primarily target the epithelial cells of the gas-exchanging alveoli, alveolar type 2 and type 1 cells (AT2s and AT1s). Two broad regenerative pathways are simultaneously engaged to repair the alveoli: functionally beneficial regeneration of the alveolar epithelium and dysplastic alveolar remodeling. AT2s and club-like progenitor cells residing near the bronchoalveolar duct junction (distal club cells/bronchoalveolar stem cells [BASCs]) are the primary players in functionally beneficial (i.e., “euplastic”) regeneration, during which they proliferate and differentiate into AT1s,[1–5] restoring the gas-exchanging alveolar epithelium. Following diffuse alveolar damage in which AT2s are ablated, dysplastic repair engages a rare population of basal cell-like $p63^+$ progenitor cells present in the intrapulmonary airways, which undergo widespread migration into the alveolar compartment and generate ectopic bronchiolar-like airway epithelium. This dysplastic bronchiolization persists indefinitely as honeycomblike cysts[6,7] that do not appear to

contribute to lung function, instead inhabiting alveolar space where functionally beneficial regeneration might otherwise occur. This maladaptive repair by intrapulmonary p63$^+$ progenitors is similar to honeycombing seen in humans with interstitial lung disease,[6,8,9] acute respiratory distress syndrome and diffuse alveolar damage,[10] and COVID-19,[11–13] in which dysplastic bronchiolization forms ectopically in the alveoli. The loss of alveolar epithelium and the failure of ectopic bronchiolized tissue to resolve over time suggest that while it probably aids in barrier restoration in the short term, this dysplastic repair is ultimately maladaptive, likely contributing to the long-term compromise of pulmonary function seen in some survivors of severe pulmonary injury.[14–18]

While the vast majority of intrapulmonary p63$^+$ progenitors contribute to dysplastic alveolar remodeling and either remain as p63$^+$ Krt5$^+$ basal cells or differentiate into mature airway lineages, lineage-tracing experiments have demonstrated the exceedingly rare contribution of post-injury intrapulmonary p63$^+$ progenitors to surfactant protein C (SPC)$^+$ AT2s in the alveoli,[6,19] raising the possibility that dysplastic basal cells might possess some inherent plasticity. The effects of paracrine signaling pathways on dysplastic remodeling have been the focus of recent attention,[6,20–22] although little is known about the cell-intrinsic regulators necessary for dysplastic expansion or fate resolution *in vivo*. Given their long-term persistence after injury and likely contribution to jeopardized lung function, capitalizing on their limited but demonstrable plasticity and altering the fate of dysplastic cells is an attractive avenue toward promoting euplastic regeneration.

Intrapulmonary p63$^+$ progenitors are the only cells in the distal lung that express the master basal cell identity transcription factor p63. p63, specifically its predominant ΔN isoform ΔNp63, is highly expressed in basal stem cells of many proliferative epithelial tissues,[23–28] where it is a crucial driver of basal cell identity,[29] proliferation,[30,31] migration,[32–34] and differentiation.[25,29,31,35,36] While ΔNp63 exerts direct transcriptional control over these basal cell processes,[32,37–41] it can also cooperate with higher-order chromatin remodelers and histone modifiers to mediate chromatin accessibility,[42–46] bookmark tissue-specific enhancer regions,[35,47] and act as a pioneer-like factor by binding and opening inaccessible chromatin.[45,48,49] With its multitiered influence over the basal cell program and critical role in virtually all epithelial tissue contexts in which it has been studied, ΔNp63 serves as a promising target to modulate basal cell fate choice in regions of dysplastic remodeling within injured lungs.

In this study, we confirm the near-permanent persistence of dysplasia in injured murine lungs and demonstrate elevated levels of ΔNp63 in injured mouse and human basal cells, including in the context of COVID-19. We further define the foundational role of ΔNp63 in the activation and maintenance of intrapulmonary basal p63$^+$ progenitors, demonstrating that loss of ΔNp63 blunts the dysplastic remodeling program by restricting intrapulmonary p63$^+$ progenitor migration and immobilizing them in the airways. We provide evidence that by alleviating the basal cell transcriptional module conferred by ΔNp63, intrapulmonary p63$^+$ progenitors can be “pushed” toward appropriate alveolar epithelial cell fates *in vitro* and *in vivo*, due to ΔNp63 knockout potentiating multiple differentiation trajectories via rewiring of the epigenetic landscape. Taken together, our findings elucidate the role of ΔNp63 in post-injury basal cells and the dysplastic remodeling program, demonstrating that

the basal cell program can be reversed and the plasticity of intrapulmonary p63$^+$ progenitors unlocked, making ΔNp63 an attractive therapeutic candidate for individuals with severe pulmonary injuries.

RESULTS

Dysplastic alveolar remodeling persists indefinitely in mice

Dysplastic remodeling occurs in response to severe pulmonary injuries in mice and humans and is thought to persist as an "epithelial scar" long after the initial injury.[6,7] We confirmed that ΔNp63$^+$ Krt5$^+$ dysplastic pods remain in 100% (n = 3/3) of wild-type mice 1 year post infection with the H1N1 influenza A virus (IAV) strain PR8 (Figures 1A and 1A′), a widely utilized strain that recapitulates many aspects of severe influenza-induced pneumonia and respiratory distress. We found proliferating Krt5$^+$ Ki67$^+$ dysplastic cells in all surveyed mice 1 year post infection (Figures 1B–1D′), confirming that these cells self-renew to maintain their foothold in injured alveolar regions long after the initial injury. The endurance of dysplasia was accompanied by significantly reduced oxygen saturation as assessed by pulse oximetry (Figure 1E), reflecting the chronic physiological consequences of severe alveolar injury.

Intrapulmonary p63$^+$ progenitors are not directly infected by influenza A virus

Intrapulmonary p63$^+$ cells are very rare in uninjured lungs but expand dramatically upon injury, suggesting they may be resistant to influenza infection. To determine whether these cells are initially infected, we utilized an engineered PR8 strain expressing a copy of Cre recombinase (IAV-Cre).[52,53] When administered to lineage reporter mice, cells that are actively infected by an IAV-Cre virion will express Cre recombinase, allowing for lineage tracing of infected cells (Figure S1A). At the early infection time points of days 3 and 7 post infection of an ai14tdTomato (RFP) mouse, IAV-Cre-mediated lineage tracing was found in SPC$^+$ AT2s and RAGE$^+$ AT1s in the alveoli (Figures S1B and S1D) and acetylated tubulin (acTub)$^+$ multiciliated and Scgb3a2 (3a2)$^+$ club cells in the airways (Figures S1C and S1E). At day 28 post infection, we observed large IAV-trace$^+$ alveolar regions comprised mostly of SPC$^+$ AT2s and RAGE$^+$ AT1s in both moderately damaged zones (Figure S1F) and areas of relatively little or no apparent injury (Figure S1G). Similarly to earlier time points, IAV-trace$^+$ 3a2$^+$ club and IAV-trace$^+$ acTub$^+$ multiciliated cells were observed in the airways at day 28 post infection (Figure S1H). The vast majority of Krt5$^+$ dysplastic cells in IAV-Cre-infected mice were untraced (Figures S1I–S1I″), although rare IAV-trace$^+$ Krt5$^+$ regions were observed (Figure S1J), suggesting that intrapulmonary p63$^+$ progenitors are not the primary target of PR8 and escape initial infection, although rare cells that are infected are able to clear virus and survive indefinitely. AT2s were the most abundantly labeled cells within the alveoli at days 3 and 28 post infection whereas AT1s bore a higher fraction of labeled cells at day 7 post infection (Figure S1K), while multiciliated cells were preferentially labeled at days 3 and 7 post infection with a shift toward club cells at day 28 post infection (Figure S1L). Quantifying the total amount of IAV-trace in either the airways or alveoli at each time point, we found that the airways were initially preferentially infected but that the IAV-trace pool shifted toward the alveolar compartment over the course of regeneration (Figure S1M). Despite being traced with somewhat similar frequencies among

cells in their respective compartments, SPC$^+$ AT2s represented a larger fraction of the total IAV-trace$^+$ pool across both compartments at day 28 post infection as opposed to 3a2$^+$ club cells, supporting the alveolar bias of IAV-trace cells at later injury time points (Figure S1N).

p63 expression is increased in injured mouse and human basal cells

We next sought to uncover cell-intrinsic molecular drivers of the expansion and maintenance of dysplastic remodeling after pulmonary injury. The basal cell transcription factor ΔNp63 is well known for maintaining basal cell identity and promoting many basal cell processes including proliferation, migration, and differentiation. Since intrapulmonary p63$^+$ progenitors are the only cells in the distal lung that express ΔNp63, we chose to investigate the role of ΔNp63 in intrapulmonary p63$^+$ progenitors and their contribution to dysplasia. Using p63^{CreERT2} mice[19,21] to lineage trace and isolate intrapulmonary p63$^+$ progenitors during injury, we found that these cells proliferate dramatically over the course of injury and repair, ultimately encompassing almost 10% of cells marked by airway epithelial integrin β4 (β4) (Figure 1F). Furthermore, ΔNp63 expression increased dramatically on a "per-cell" basis as dysplastic basal progenitors expanded ectopically into the alveoli, reaching its peak surveyed expression by day 21 post flu (Figure 1G). To determine whether p63 expression similarly increased in injured human basal cells, we reanalyzed single-cell RNA sequencing (RNA-seq) datasets from healthy and idiopathic pulmonary fibrosis (IPF) human patient lung tissue samples.[50] p63 expression is restricted to two epithelial populations within this dataset: basal cells and a population identified as Krt5$^-$/Krt17$^+$ cells (Figures 1H and 1I), a basal-like population largely restricted to diseased patient samples and associated with both "transitional" AT2s in mice and humans, and transdifferentiation of AT2s into basaloid cells in humans.[54–57] We confirmed that p63 expression is significantly elevated in human basal cells (Figure 1J) and Krt5$^-$/Krt17$^+$ cells (Figure 1K) from IPF patients compared with healthy donors, indicating that p63 expression is dynamically regulated in both mouse and human lungs upon injury. We also observed strong p63 staining in the Krt5$^+$ cells that line dysplastic epithelial cysts in the alveoli of human patients with a variety of pulmonary injuries and diseases, including IPF (Figure 1M), familial IPF (Figure 1N), scleroderma (Figure 1O), and COVID-19 (Figures 1P and 1Q), but not in the alveolar regions of healthy patients (Figure 1L), further highlighting the potential relevance of p63 in human lung disease.

Broad airway epithelial ΔNp63 deletion attenuates dysplastic alveolar remodeling

Since the dysplastic cell of origin resides in the intrapulmonary airways,[21,58] we asked whether broad ΔNp63 deletion in the airway epithelium could attenuate Krt5$^+$ dysplasia following influenza injury *in vivo*. Utilizing Sox2^{CreERT2} mice bearing RFP and ΔNp63^{flox} alleles, we simultaneously lineage traced and deleted ΔNp63 in the airway epithelium.[59–61] Sox2^{CreERT2};RFP (Sox2^{ΔNp63WT}) and Sox2^{CreERT2};RFP;ΔNp63$^{flox/flox}$ (Sox2^{ΔNp63KO}) mice were administered a single dose of intraperitoneal (i.p.) tamoxifen and infected with PR8 (Figure 2A). In mock injured control mice, the Sox2-trace is almost exclusively restricted to the airway epithelium as previously described,[21,58] observing only rare labeled SPC$^+$ AT2s in the alveoli (Figures S2A–S2C). Importantly, Krt5$^+$ basal cell expansion was not observed in the airways or alveoli under mock injury conditions, and as such was not labeled by the Sox2^{CreERT2} (Figures S2A and S2C). While injured Sox2^{ΔNp63WT} mice

had large expansions of Sox2-trace^{+} Krt5^{+} dysplasia consistent with their severe damage (Figure 2B), Sox2$^{\Delta Np63KO}$ mice did not display any Krt5^{+} dysplasia (Figure 2C), prompting us to examine the lineage contributions that Sox2$^{\Delta Np63WT}$ and Sox2$^{\Delta Np63KO}$ mice make to alveolar repair. Consistent with previous reports,[21,58] influenza-injured Sox2$^{\Delta Np63WT}$ mice contained many Sox2-trace^{+} SPC^{+} AT2s (Figure 2D) and Sox2-trace^{+} RAGE^{+} AT1s (Figure 2E) in the alveoli along with Sox2-trace^{+} Krt5^{+} dysplasia (Figure 2F) expressing high levels of p63 (Figure S2E) at day 21 post flu, likely originating from injury-activated distal club cells/BASCs[4,5,62] and intrapulmonary p63^{+} progenitors,[6,21,63] respectively. Sox2-trace^{+} expansion into SPC^{+} AT2s was occasionally observed in alveolar regions with little obvious injury (FigureS2D). p63 expression inSox2-trace^{+} regions was present in injured Sox2$^{\Delta Np63WT}$ mice (Figure S2E) but completely abrogated in Sox2$^{\Delta Np63KO}$ mice upon ΔNp63 deletion prior to injury (FigureS2F). While regions of Sox2-trace^{+} SPC^{+} (Figure 2G) and Sox2-trace^{+} RAGE^{+} (Figure 2H) alveolar expansion persisted in Sox2$^{\Delta Np63KO}$ mice, Sox2-trace^{+} Krt5^{+} dysplastic alveolar regions were exceedingly rare (Figure 2I), indicating that ΔNp63 is necessary for airway epithelial cells to contribute to maladaptive alveolar remodeling. Comparing capillary oxygen saturation measured via pulse oximetry, Sox2$^{\Delta Np63KO}$ mice retained elevated blood oxygenation ability at day 9 post infection and recovered to a greater degree by day 28 post infection compared with their Sox2$^{\Delta Np63WT}$ counterparts (Figures 2K and 2L), suggesting that dysplastic Krt5^{+} repair could indeed be maladaptive and that regeneration of the alveolar epithelium is enhanced in the absence of dysplasia.

ΔNp63^{KO} lung basal progenitors fail to migrate from airways

In addition to attenuated dysplastic alveolar remodeling, Sox2$^{\Delta Np63KO}$ mice had an approximately 2-fold increase in the relative percentage of Sox2-trace^{+} SPC^{+} AT2s compared with Sox2$^{\Delta Np63WT}$ mice (Figure 2J). To address the possibility that ΔNp63^{KO} intrapulmonary basal cells can participate in euplastic AT2 regeneration, we utilized p63^{CreERT2} mice to simultaneously lineage trace and delete ΔNp63 specifically in basal cells prior to injury. While i.p. tamoxifen caused no unexpected side effects in uninjured p63^{CreERT2};RFP (p63$^{\Delta Np63WT}$) mice, administering a single dose of i.p. tamoxifen to uninjured p63^{CreERT2};RFP; ΔNp63^{flox} (p63$^{\Delta Np63KO}$) mice was lethal within 5–7 days, likely because ΔNp63 deletion causes severe defects in epithelia that rely on basal cells for homeostatic maintenance (e.g., skin).[23–25,29,31,39,40,64] To circumvent this lethality, we intranasally administered three doses of 4-hydroxytamoxifen (4OHT) sonicated into PBS to p63$^{\Delta Np63WT}$ and p63$^{\Delta Np63KO}$ mice. p63$^{\Delta Np63KO}$ mice treated with this method survive the full tamoxifen dosing, ≥1 week chase period, and subsequent injury time course with minimal side effects (Figure 3A). In mock injury control mice, ΔNp63^{+} p63-trace^{+} cells are found in the basal layer of the intrapulmonary airways (Figure S3A), where they are rare and scattered, and absent in the alveoli (Figure S3B), all as previously described.[19,21] As expected, p63-trace^{+} regions were found at day 21 post flu within p63$^{\Delta Np63WT}$ airways and alveoli (Figure 3B) as previously described.[19,21] In stark contrast, p63-trace^{+} cells were restricted to the airways of p63$^{\Delta Np63KO}$ mice and did not extend into the alveolar space when ΔNp63 was deleted before injury (Figure 3C). We observed a dramatic reduction in the number of p63-trace^{+} cells in both the airways and alveoli of p63$^{\Delta Np63KO}$ mice (Figure 3D), underscoring the near-complete abolishment of intrapulmonary p63^{+} progenitor expansion

without ΔNp63.Occasional p63-trace^{+} cells in the airways of p63$^{-\Delta}$ Np63KO mice still expressed ΔNp63 (Figures S3C and S3E) and Krt5 (Figures S3D and S3F) similarly to p63$^{\Delta Np63WT}$ mice, indicating incomplete recombination of the ΔNp63^{flox} allele. Capillary oxygen saturation was not significantly different between p63$^{\Delta Np63WT}$ and p63$^{\Delta Np63KO}$ mice (Figure S3G), likely due to incomplete ΔNp63^{flox} allele recombination and the fact that p63^{CreERT2} mice already exhibit haploinsufficiency for p63,[19] although p63$^{\Delta Np63KO}$ mice did trend toward higher oxygen saturation at later time points consistently with the more significant changes observed with Sox2^{CreERT2}-mediated ΔNp63 deletion (Figures 2K and 2L). In total, these results demonstrate that the increased percentage of Sox2-trace^{+} SPC^{+} AT2s is not due to direct conversion of ΔNp63^{KO} intrapulmonary basal progenitors into AT2s and that ΔNp63^{KO} intrapulmonary basal progenitors fail to contribute to Krt5^{+} dysplasia.

Recognizing that the failure of ΔNp63^{KO} mice to mount a dysplastic remodeling response could be caused by attenuated migration from the airways, we assessed the impact of ΔNp63 deletion on basal cell migration *in vitro*. Adding the basal cell-specific cell surface marker lymphocyte antigen 6 family member D (Ly6D) (Figures S4A and S4B) to previously established sort schemes,[6,65] we were able to sort enriched intrapulmonary p63^{+} progenitors from day 14 post-flu non-tamoxifen-treated Krt5^{CreERT2};RFP;ΔNp63$^{flox/flox}$ (Krt5$^{\Delta Np63KO}$) mice, allowing for inducible deletion of ΔNp63 *in vitro* with 4OHT. Seeding the cells yielded from this sorting strategy as organoids followed by adaptation to monolayer conditions effectively enriches for a highly pure basal cell population from post-flu mice expressing both p63 and Krt5 (Figures S4C and S4D). Using these cells for migration assays, dimethyl sulfoxide (DMSO)-treated (−4OHT) monolayer gap areas were reduced by 6 h post insert removal, with gap areas fully closed by 24 h (Figures 3E, 3E″, and 3G). In contrast, 4OHT-treated (+4OHT) monolayer migration was significantly impeded, evidenced by only a slight gap-area reduction by 6 h and failure to fully close the gap by 24 h (Figures 3F, 3F″, and 3G). Comparing the derived rate of gap-area closure over the initial 6 h window, 4OHT-treated monolayers migrated significantly slower than their DMSO-treated counterparts (Figure 3H), substantiating the hypothesis that ΔNp63^{KO} intrapulmonary basal progenitors are unable to execute a migratory program and thus cannot participate in dysplastic alveolar remodeling following *in vivo* deletion.

Pro-alveolar histone modifications and transcriptional changes occur with ΔNp63 deletion

p63 directly promotes the basal cell program and actively enforces basal cell identity transcriptionally[25,29,32,38,40,66] and epigenetically,[35,43,46–48] thereby causing precocious terminal differentiation of basal cells when deleted or inhibited.[19,29,31,32,36,39] Reasoning that the observed decrease in migratory capacity could be a reflection of fundamental changes in the epigenome with ΔNp63 loss, we surveyed the epigenetic and transcriptomic landscapes of ΔNp63^{KO} intrapulmonary basal progenitors via chromatin immunoprecipitation sequencing (ChIP-seq) and RNA-seq, respectively, hypothesizing that ΔNp63 deletion might promote enrichment of active and/or depletion of repressive histone marks around the genomic loci of lung identity and airway/alveolar epithelial differentiation genes and accompanying inverse changes around basal cell gene loci (Figure 4A). We performed p63, H3K27ac (associated with open chromatin and transcriptional activation),

and H3K27me3 (associated with closed chromatin and transcriptional repression) ChIP-seq on post-flu Krt5^{+} cells isolated from a non-tamoxifen-treated Krt5$^{\Delta Np63KO}$ mouse. Monolayers for ChIP-seq were treated with DMSO (no ΔNp63 deletion, yielding Krt5$^{\Delta Np63WT}$ cells used for p63, H3K27ac, and H3K27me3 ChIP-seq) or 1 μM 4OHT (ΔNp63 deletion, yielding Krt5$^{\Delta Np63KO}$ cells used for H3K27ac and H3K27me3 ChIP-seq) for 48 h, immunoprecipitated, and sequenced. All samples had ≥11 million reads mapped to the mouse genome with a ≥96% alignment rate (Figure S5A). p63 binding was found mostly in promoters and distal intergenic regions (e.g., enhancers) as previously described[47,67] as well as within early introns and transcriptional start sites (TSSs) (Figures 4B and S5B), and our p63 ChIP-seq dataset recapitulated known p63 binding sites upstream of the Krt5 TSS (Figure S5I).[40,68] H3K27ac and H3K27me3 ChIP-seq revealed dramatic rewiring of the epigenetic landscape between Krt5$^{\Delta Np63WT}$ and Krt5$^{\Delta Np63KO}$ cells (Figures S5C and S5D). We found 13,733 differentially enriched H3K27ac peaks between Krt5$^{\Delta Np63WT}$ and Krt5$^{\Delta Np63KO}$ cells with a significant decrease in H3K27ac (i.e., chromatin closing) at proximal (≤1 kb from TSS) promoters and a significant increase in H3K27ac (i.e., chromatin opening) at distal intergenic regions in Krt5$^{\Delta Np63KO}$ cells (Figures 4C, S5E, and S5G), and 5,838 differentially enriched H3K27me3 peaks between Krt5$^{\Delta Np63WT}$ and Krt5$^{\Delta Np63KO}$ cells with no significant trend toward any annotated genomic regions (Figures 4D, S5F, and S5H). Interestingly, ~30%of p63-bound regions become enriched in H3K27ac upon ΔNp63^{KO} (Figure 4E). On the other hand, only 0.44% of p63-bound regions become depleted of H3K27ac, 0.34% of p63-bound regions become enriched in H3K27me3, and no regions are both bound by p63 and become depleted of H3K27me3 upon ΔNp63^{KO} (Figure 4E). *De novo* transcription factor motif enrichment analysis detected p53 family members such as p63 itself, FOX family, and Sp/KLF family transcription factor motifs enriched within p63-bound sequences (Figure 4F); many binding motifs of members of these same transcription factor families were also detected within enriched and depleted H3K27ac and H3K27me3 regions upon ΔNp63^{KO} (Figures 4G–4J), with notable repeated detection in multiple categories of Foxj3, Sp5, Wt1, and Maz in particular, suggesting coordinated transcriptional and epigenetic regulation of basal cell identity between these transcription factor families.

Among the most dramatic dynamic changes in epigenetic modification were exhibited by the key lung epithelial identity transcription factor Nkx2-1, which became enriched in H3K27ac along its entire gene body upon ΔNp63^{KO} (Figure 4K), indicating enhanced open chromatin and poising for transcriptional activation. Surprisingly, we detected a p63 binding site within exon 2 of Nkx2-1; following ΔNp63^{KO}, the region surrounding this binding site becomes the most significantly H3K27ac-enriched region of the entire Nkx2-1 locus and is among the top 20% of the most highly differentially enriched H3K27ac regions with ΔNp63^{KO} in our entire dataset (Figure 4K), strongly suggesting that p63 exerts a repressive influence over Nkx2-1. Considering that post-injury basal-like progenitors can rarely differentiate into AT2s following their migration into the alveoli[21] and the increased H3K27ac around the Nkx2-1 locus, we turned our attention toward changes in epigenetic marks at other alveolar differentiation loci. Similarly to Nkx2-1, we found a p63 binding site in the putative promoter of the lung epithelial development and repair transcription factor Id2,[69] which also gains H3K27ac across its gene body following ΔNp63^{KO} (Figure

4L). Additional loci without obvious p63 binding also underwent dynamic changes in their histone composition, including the AT1 markers Hopx (Figure S5J) and Aqp5 (Figure S5K), the AT2 marker Abca3 (Figure 4M), and Klf5 (Figure S5L), which has recently been implicated in AT2 differentiation and fate choice,[70] which were all highly enriched in H3K27ac at their transcriptional and translational start sites with $\Delta Np63^{KO}$. Conversely, $\Delta Np63^{KO}$ cells exhibited enhanced H3K27me3 across the gene bodies of regulators of basal cell processes such as Twist1 (Figure 4N) for epithelial-to-mesenchymal transition (EMT)[71] and Hes5 (Figure S5M) for Notch signaling, indicating epigenetic repression of these cellular programs and signaling pathways. In total, these results indicate that ΔNp63 maintains the epigenome of intrapulmonary $p63^{+}$ progenitors in a specific pro-basal cell configuration and that loss of ΔNp63 may allow for rewiring of the epigenetic landscape into one amenable to alveolar differentiation.

These epigenetic changes prompted us to assess gene expression changes via RNA-seq of basal cell monolayers treated in parallel with those used for ChIP-seq, in which $\Delta Np63^{KO}$ induced significant changes in the basal cell transcriptome (Figure S5N and S6A). Consistent with the role of ΔNp63 in maintaining basal cell identity, many canonical basal cell markers were significantly reduced upon $\Delta Np63^{KO}$ (Figure 4O). Consistent with our ChIP-seq data, expression levels of lung and alveolar epithelial identity transcription factors including Nkx2-1 and Hopx increased with $\Delta Np63^{KO}$ while the airway epithelial identity transcription factor Sox2 expression was significantly downregulated (Figure 4P), indicating a shift toward a more distal airway/alveolar fate.

Considering the vast morphological, transcriptional, and anatomical differences between basal cells and AT2s, in addition to the rarity of intrapulmonary basal progenitor-to-AT2 differentiation *in vivo*, we hypothesized that $\Delta Np63^{KO}$ intrapulmonary basal progenitors might pass through an intermediary cell type common to both lineages. Since tracheal basal cells can differentiate into club cells during airway homeostasis and repair, and distal club cells/BASCs can differentiate into AT2s, we predicted that $\Delta Np63^{KO}$ intrapulmonary basal progenitors might assume a distal club cell/BASC-like phenotype. In line with this prediction, canonical club cell secretoglobin expression was downregulated in favor of a set of distal club cell/BASC markers including many major histocompatibility complex class I and II genes (Figure 4Q). Consistent with assumption of the distal club cell/BASC-like phenotype and progenitor properties associated with it, $\Delta Np63^{KO}$ monolayers upregulated some, but not all, mature AT2 markers such as SPD and Abca3 (Figure 4R), again reflecting the enrichment of H3K27ac at alveolar loci found via ChIP-seq. Expression of most mature airway markers was unchanged (Figure 4S), confirming that $\Delta Np63^{KO}$ basal cells do not spontaneously commit to these airway lineages in monolayer conditions. These findings indicate that $\Delta Np63^{KO}$ allows basal cell monolayers to transition toward an intermediate club/AT2like fate, sharing transcriptional similarities with both cellular identities without fully differentiating into mature airway cell types.

ΔNp63 deletion induces intrapulmonary basal progenitor plasticity

Given the transcriptional shift toward an alveolar fate with $\Delta Np63^{KO}$ as monolayers, we moved to an organoid culture system, since these conditions are known to support higher

efficiency of AT2 generation.[72,73] Immunostaining reflected the conversion of ΔNp63^{KO} intrapulmonary basal progenitor organoids into AT2-like cells when maintained in alveolar medium, asKrt5 protein expression decreased with ΔNp63^{KO} (Figures 5A and 5B) and was replaced with punctate SPC staining in many organoids (Figures 5C and 5D). RNA-sequencing of ΔNp63^{WT} and ΔNp63^{KO} organoids maintained in either airway or alveolar medium revealed a dramatic transcriptional shift similarly to monolayers (Figures 5E, 5F, S6B, and S6C). ΔNp63 deletion diminished basal cell identity as expected in organoids maintained in either organoid condition (Figures 5G and 5H). In contrast to monolayer conditions, airway epithelial differentiation was more pronounced in three-dimensional (3D) culture; in airway medium conditions, ΔNp63^{KO} organoids assumed a multiciliated/tuft cell-like transcriptional signature (Figure 5I) whereas minimal shifts toward mature airway cell types—with the exception of multiciliated cell differentiation—were observed in alveolar medium conditions (Figure 5J), reinforcing a model wherein differentiation of these cells is dependent upon a combination of p63 expression, culturing method (i.e., 2D versus 3D), and medium conditions/niche cues. ΔNp63^{KO} organoid maintenance in airway medium allowed for expression of distal club/BASC markers at the expense of mature club cell markers (Figure 5K), and culturing ΔNp63^{KO} organoids in alveolar medium induced an even stronger distal club/BASC signature (Figure 5L). Interestingly, ΔNp63^{KO} airway organoids upregulated some AT2 markers such as the surfactant proteins SPA and SPD and lysozymes Lyz1 and Lyz2 (Figure 5M), perhaps reflecting the promiscuous expression of surfactant, lysosomal, and secretory-associated genes seen in distal club cells/BASCs.[4,5,74] Strikingly, ΔNp63^{KO} alveolar organoids robustly differentiated into AT2s, evidenced by significant upregulation of a suite of canonical mature AT2 markers including nearly all surfactant proteins with the exception of SPC, whose p value was slightly below the significance threshold ($p = 0.085$), genes involved in surfactant production such as Lamp3, Abca3, and Lpcat1, and lysosomal genes Lyz1 and Lyz2 (Figure 5N). Subjecting ΔNp63^{KO} organoids to airway or alveolar medium conditions revealed the plasticity afforded by ΔNp63 deletion, confirming that ΔNp63^{KO} basal-like cells adopt increased plasticity, similarly to distal club/BASCs, and can subsequently respond to external cues favoring either airway or alveolar differentiation.

ΔNp63^{KO} intrapulmonary basal progenitors differentiate into AT2s *in vivo*

Given that p63 deletion in pro-alveolar medium promoted differentiation into cells provocatively similar to AT2s, we attempted to assess the effects of ΔNp63 deletion *in vivo* after dysplastic expansion. However, despite many attempts with different Cre drivers and routes of tamoxifen delivery, we were unable to achieve full ΔNp63 deletion in the post-flu dysplastic regions with either i.p. or intranasal tamoxifen delivery (Figures S7A–S7D). Attempts to increase recombination by raising the dose of tamoxifen or 4OHT invariably resulted in animal death as earlier described. To circumvent these issues, we utilized an orthotopic transplantation strategy in which bulk β4^{+} airway cells from influenza-injured Krt5^{CreERT2};RFP;ΔNp63$^{flox/-}$ (Krt5^{ΔNp63HET}, serving as wild-type controls) or Krt5^{ΔNp63KO} donors were intranasally transplanted into injured CreERT2^{negative} littermates (Figure 6A). Following engraftment and i.p. tamoxifen administration, we were able to assess the fate potential of ΔNp63^{KO} intrapulmonary basal progenitors *in vivo*. The ΔNp63^{flox} allele was able to be fully recombined utilizing this method (Figures S8A and S8B), likely

due to our ability to give a full i.p. tamoxifen course while avoiding lethality in the recipient mice. Consistent with their dysplastic basal-like phenotype, the majority of $Krt5^{\Delta Np63HET}$ engraftments formed $Krt5^{+}$ pod-like structures (Figures 6B and 6H) although rare engraftments contained scarce SPC^{+} AT2s (Figures 6C and 6I), in line with the infrequent observation of AT2 differentiation from dysplastic cells.[6] On the other hand, $Krt5^{\Delta Np63KO}$ engraftments rarely expressed Krt5 (Figures 6D and 6H), instead more readily converting into SPC^{+} AT2s than their $Krt5^{\Delta Np63HET}$ counterparts (Figures 6E and 6I). These SPC^{+} engraftments additionally expressed Lamp3 (Figure 6F) and the AT1 marker RAGE (Figure 6G), supporting the conclusion that the plasticity conferred to intrapulmonary basal progenitors via $\Delta Np63^{KO}$ allows them to differentiate into AT2s, which then assume their role as a bona fide progenitor population and further differentiate into AT1s at the expense of airway cell types *in vivo*.

DISCUSSION

Multiple caveats exist to the traditional pulmonary epithelial progenitor hierarchy and existing paradigms of lung repair. For example, genetic ablation of basal cells in the trachea induces committed club cells to de-differentiate into basal cells, which can then respond to airway insults as endogenous basal cells would.[75] In humans this plasticity appears to be bidirectional, as AT2s can be driven to aberrantly transdifferentiate into basal cells when exposed to transforming growth factor β signaling from altered mesenchymal niche cells that arise in diseased lungs.[57] Our study provides further nuance to these models, in which dysplastic basal-like cells can be converted into AT2s with loss of the basal cell identity transcription factor ΔNp63. While these findings challenge aspects of lung lineage restriction and terminal differentiation models, they also provide mechanisms that can be leveraged to modulate pulmonary repair.

Despite the detrimental nature of long-term alveolar inhabitation by dysplastic tissue, alveolar re-epithelialization by intrapulmonary $p63^{+}$ progenitors is thought to be critical for the short-term survival of individuals with severe injuries, owing to the rapid restoration of pulmonary barrier function. Interestingly, our data suggest that pulmonary injury is not only survivable in the absence of dysplastic repair (via ΔNp63 loss) but that dysplasia itself is maladaptive and exacerbates pulmonary injuries, as mice with no dysplasia become less hypoxic following influenza infection and recover to a greater extent than their wild-type counterparts. Some studies suggest that failure to mount a dysplastic response is detrimental to the recovery of lung function, as genetic ablation of dysplastic cells in influenza-injured mice causes persistent inflammation, fibrosis, and a failure to recover normal blood oxygen saturation levels.[76] Given that dysplastic bronchiolization appears to be evolutionarily conserved,[6,7] we predict that it does indeed provide some survival benefit within a window of very severe injury, although proving this will require precise control of injury levels and cell-type-specific ablation techniques.

The mechanisms by which cells acquire, maintain, and alter their identity are critical to understanding how and why progenitor populations respond to injury and contribute to disease states.[54,56,77,78] Our data provide a direct mechanism for ΔNp63 in maintaining the basal cell identity of intrapulmonary $p63^{+}$ progenitors, in which ΔNp63 modulates

fate by regulating histone modifications at loci required for distal airway and alveolar differentiation, such as Nkx2-1 and Id2. Interestingly, the p63 binding site we report for Nkx2-1 is in its second exon. Considering that exonic transcription factor binding is thought to tightly modulate the transcriptional output of bound loci[79–82] and our observation that H3K27ac around and transcriptional levels of Nkx2-1 increases without p63, we speculate that p63 binding at this site allows for coordination of cell identity via interplay between these important cell-fate-conferring genes. While we show direct regulation by p63 of some alveolar differentiation loci (Nkx2-1 and Id2), other loci which lack p63 binding also exhibit dramatic changes in their histone composition (e.g., Hopx, Aqp3, Abca3), indicating indirect regulation of the epigenetic landscape by p63 as well. Considering this, it is additionally likely that p63 cooperatively exerts its epigenetic control over these loci with as yet unidentified lung-tissue-specific and cell-specific transcription factors, chromatin remodelers, and histone modifiers as it does in other epithelial tissues.[42,47,67] Our data strongly suggest that p63-mediated histone deacetylase (HDAC) recruitment could be one such important mechanism at play in intrapulmonary $p63^{+}$ progenitor maintenance given that H3K27ac enrichment accounted for the majority of changes in histone modifications we saw with $\Delta Np63^{KO}$, which would presumably lead to reduced HDAC recruitment to those loci.[83] Identification of these epigenetic factors may represent promising druggable targets for *in vivo* directed differentiation to convert $p63^{+}$ progenitors into functionally beneficial AT2s and AT1s.

Our data suggest that the differentiation trajectory of $\Delta Np63^{KO}$ basal cells can be modulated depending on their location (airway or alveoli) and the timing of ΔNp63 deletion (before or after injury). We found that ΔNp63 deletion prior to injury renders intrapulmonary $p63^{+}$ progenitors restricted to the airways, and our organoid experiments suggest that they differentiate into club, ciliated, and tuft cells, a concordant finding with the differentiation trajectory of embryonic $p63^{KO}$ airway basal cells.[19] Conversely, if injury-activated basal progenitors are in the alveolar compartment when they lose ΔNp63 expression, they upregulate mature AT2 genes at the expense of airway cell markers both *in vivo* with orthotopic transplantation and when maintained in alveolar organoid conditions. Interestingly, $\Delta Np63^{KO}$ intrapulmonary basal progenitor organoids express a core set of distal club/BASC genes, which we propose constitutes a “ground state” for an intrapulmonary basal progenitor that loses its basal cell identity. This model parsimoniously allows $\Delta Np63^{KO}$ intrapulmonary basal progenitors to exist in an intermediate state along the pulmonary epithelial cell hierarchy, poised toward further airway or alveolar differentiation depending on encountered signals. Whether this is a discrete, definable state *in vivo* or rather represents a relative and dynamic position on a differentiation spectrum remains to be determined.

Histone modifications at alveolar identity and differentiation loci, including the transcription factors Nkx2-1, Id2, Klf5, and Hopx,[70,84–88] and AT2- and AT1-specific genes themselves, change significantly with ΔNp63 knockout. Considering that differentiation into alveolar cells is a dramatic shift in identity that rarely happens *in vivo*, $\Delta Np63^{KO}$ intrapulmonary basal progenitors likely require larger-scale epigenetic rewiring and chromatin remodeling to proceed down this differentiation path. This, coupled with enrichment of repressive histone modifications around regulators of basal cell function and identity including EMT

and the Notch pathway with $\Delta Np63^{KO}$, further indicates that ΔNp63 actively maintains chromatin in a configuration amenable to basal cell maintenance and airway differentiation and that the rare *in vivo* event of native intrapulmonary $p63^+$ progenitor differentiation into AT2s requires lowered ΔNp63 expression levels. Indeed, our orthotopic transplantation model confirms that $\Delta Np63^{KO}$ intrapulmonary basal progenitors convert into AT2s *in vivo* more readily than their ΔNp63-expressing counterparts; however, rare $Krt5^{\Delta Np63HET}$ SPC^+ intrapulmonary $p63^+$ progenitor engraftments suggest that even intrapulmonary $p63^+$ progenitors with sustained ΔNp63 levels exhibit a level of innate plasticity that can be influenced by the surrounding microenvironment. The intracellular mechanisms or extracellular signals that reduce ΔNp63 expression, thereby altering chromatin organization and allowing for plasticity, remain unknown and warrant further study.

This study identifies ΔNp63 as a critical driver of dysplastic alveolar remodeling and elucidates mechanisms that promote intrapulmonary $p63^+$ progenitor plasticity, allowing for their differentiation into AT2s. The dramatic regulation of dysplastic remodeling and epigenetic control of lung identity by ΔNp63 expands on our knowledge of lung progenitor cell biology, plasticity, and roles in injury repair, providing nuance to the interconnected lung epithelial cell hierarchy and the ability of vastly different lung progenitors to converge upon similar cell states. Given that ΔNp63 expression is associated with diseased states in both mice and humans and our *in vivo* mouse data exhibiting enhanced lung repair in the absence of ΔNp63, the governance of lung regeneration and cell identity demonstrated in this work highlights exciting avenues for the development of therapies to treat patients afflicted with a wide array of severe pulmonary injuries and diseases that involve dysplastic alveolar remodeling, including interstitial lung disease, IPF, diffuse alveolar damage, and COVID-19.

Limitations of the study

Our work finds that the inherent plasticity of intrapulmonary basal-like progenitors in the regenerating lung can be expanded by alleviating the basal cell fate driver ΔNp63, allowing for basal cell differentiation into appropriate alveolar epithelial cell types such as AT2s and AT1s. A significant limitation of this study was our inability to efficiently delete ΔNp63 strictly and specifically in lung basal cells *in vivo*, which will require yet-to-be-developed lung dysplastic basal cell lineage drivers that are active solely in these cells. While we present evidence that ΔNp63 directly exerts epigenetic control of some alveolar differentiation genes, it is likely that ΔNp63 also maintains an indirect epigenetic influence over different loci via cooperation with other epigenetic modifiers and enzymes, and our data agree strongly with reports showing that ΔNp63 can cooperate with multiple chromatin remodeling enzymes[49] including direct binding with HDACs.[83] Additionally, while ΔNp63 loss is sufficient to drive plasticity and conversion of basal cells into AT2s, whether ΔNp63 loss is necessary for this process is unknown; in other words, alternative transcription factors, chromatin remodelers, epigenetic factors, and signaling pathways might also constitute routes to promote divergent fates independent of ΔNp63. If this is indeed the case, some of these alternative means of inducing basal cell plasticity might be preferable to ΔNp63 from a therapeutic standpoint for human lung disease, as the importance of ΔNp63 in the homeostatic maintenance of numerous organs throughout the

body renders ΔNp63 a poor target. As such, this work constitutes a proof of principle that the fate of dysplastic pulmonary basal cells can be altered into functionally beneficial alveolar cell types, although further work is needed to find suitable drug targets to achieve this same goal that also provide safe and efficacious results in clinical settings.

STAR★METHODS

RESOURCE AVAILABILITY

Lead contact—Requests for further information, reagents, and resources related to this study should be directed to Dr. Andrew Vaughan (andrewva@vet.upenn.edu).

Materials availability—Materials used in this study will be distributed upon request to the lead contact.

Data and code availability

- Bulk RNA-and ChIP-seq data have been deposited to the Gene Expression Omnibus (GEO) and are publicly available as of the date of publication under the accession number GEO: GSE216161.
- This paper does not report original code.
- Any additional information required to reanalyze the data reported in this paper is available from the lead contact upon request.

EXPERIMENTAL MODEL AND SUBJECT DETAILS

Animals and treatment—8- to 10-week-old mice were used for all experiments with males and females in roughly equal proportions. Experimenters were not blinded to mouse age or sexes. Ai14tdTomato (Gt(ROSA)26Sor$^{tm14(CAG-tdTomato)Hze}$),[59] ΔNp63^{flox,61,89} Sox2^{CreERT2} (Sox2$^{tm1(cre/ERT2)Hoch}$),[60] Krt5^{CreERT2,27} and p63^{CreERT2,90} mice have been previously described. All studies were approved by the University of Pennsylvania's Institutional Animal Care and Use Committees, protocol 806262, and followed all NIH Office of Laboratory Animal Welfare regulations. Genotyping primers for all transgenic mice used are in Table S1.

Influenza virus propagation and infection—Influenza A/H1N1/Puerto Rico/8/34 (PR8) was propagated in embryonated chicken eggs while IAV-Cre was propagated in MDCK cells, both according to established protocols.[91] Virus titration by TCID50 for infectivity titer was performed in MDCK cells for both viral strains.[91] For infection with either PR8 or IAV-Cre, mice were first anesthetized using 3.5% isoflurane in 100% O_2 via an anesthesia vaporizer system. Mice were intranasally administered (2 * bodyweight in grams) – 5 U TCID50 (ex. A 25g mouse gets (2 * 25g) - 5U = 45U) PR8 by pipetting 30μL of virus dissolved in phosphate-buffered saline (PBS) onto the nostrils of anesthetized mice in visually confirmed agonal breathing. Since IAV-Cre takes a higher dosing to achieve comparable injury,[52,53] anesthetized mice in agonal breathing were administered (8 * bodyweight in grams) TCID50 U (ex. A 25g mouse gets (8 * 25g) = 200U) IAV-Cre intranasally. Only infected mice that lost ≥10% of their starting body weight by day 9

post-flu were considered to be adequately infected with either strain and were used for all experiments involving influenza infection. Mouse weights were tracked throughout infection until the experimental endpoint. All mice that received PR8 for histology experiments were sacrificed at day 21 post-flu. All mice that received IAV-Cre for histology experiments were sacrificed at days 3, 7, and 28 post-flu. All mice that received PR8 for cell sorting were sacrificed at day 14 post-flu unless otherwise indicated.

Human tissue—Human tissue samples were obtained from either the UCSF Interstitial Lung Disease Blood and Tissue Repository (interstitial lung disease samples) or the Penn Lung Biology Institute Human Lung Tissue Bank (normal lung and COVID-19 samples) and are de-identified, otherwise discarded human tissues. COVID-19 samples were from patients who previously tested positive for COVID-19 by PCR test but tested negative via PCR test prior to tissue acquisition. All COVID-19 samples were obtained from ventilated ARDS patients who underwent lung transplant, at which time tissue samples were acquired. All samples were from adult patients and were selected randomly without regard for age or gender, only for underlying diagnosis. All information on patient sample collection for the single cell RNA-seq dataset (Figures 1H–1K) is available in Habermann et al. 2020.[50]

METHOD DETAILS

Intranasal and intraperitoneal tamoxifen administration—For intraperitoneal tamoxifen experiments, mice were injected with a single 0.25mg/g dose of intraperitoneal (IP) tamoxifen dissolved in 50μL corn oil into the intraperitoneal cavity and allowed ≥1 week for allele recombination and tamoxifen clearance prior to influenza infection. For intranasal 4OHT experiments, 0.025mg/g (E/Z)-4-hydroxytamoxifen (17,308, Cayman Chemical) of a 100mg/mL stock in DMSO was sonicated into 30μL PBS at 4°C using an S220 Focused-Ultrasonicator (Covaris) with sonication at peak power = 140, duty factor = 5, 200 cycles/burst for 60 s followed by 30 s delay for 20 cycles. Mice were then anesthetized and intranasally administered the sonicated solution according to the procedure in “Influenza infection”. Mice treated with intranasal 4OHT were given three doses every other day over the course of six days and allowed a two-week chase for allele recombination and tamoxifen clearance prior to influenza infection.

Pulse oximetry—Repeated measurements of peripheral oxygen saturation (SpO_2) were taken using a MouseOx Plus Rat & Mouse Pulse Oximeter and a MouseOx small collar sensor (Starr Life Sciences Corp.). Mice were shaved around the neck and shoulders where the collar sensor sits at least one day prior to the initial reading. Recordings were taken using MouseOx Premium Software (Starr Life Sciences Corp., Oakmont, PA, USA). Measurements were taken continuously for >3 minutes at a measurement rate of 15 Hz. Measurements were imported into Microsoft Excel and all readings with an Error Code besides “Lost Breath Rate” were discarded. The average of these readings was used to calculate the SpO_2 reading for each mouse for each given time point.

Lung tissue preparation for immunostaining—Following euthanasia, lungs were inflated with 1mL of 3.2% paraformaldehyde (PFA) and incubated in 3.2% PFA for 1 h at room temperature. Fixed lungs were then washed in multiple PBS washes over the course

of 1 hour at room temperature, followed by an overnight incubation in 30% sucrose in PBS shaking at 4°C, and then a 2-h incubation in 15% sucrose in PBS +50% OCT compound (Fisher HealthCare) at room temperature. Finally, fixed lungs were randomly oriented and embedded in OCT by flash freezing with dry ice and ethanol.

Immunostaining—All protocols were used identically for both mouse and human tissue. 7μm sections were cut on a Leica CM3050 S Research Cryostat (Leica Biosystems). Tissue sections were further fixed for 5 minutes in 3.2% PFA, rinsed three times with PBS, and blocked in blocking solution (PBS + 1% bovine serum albumin (Affymetrix) + 5% normal donkey serum (Jackson Immuno Research) + 0.1% Triton X-100 (Millipore Sigma) + 0.02% sodium azide (Millipore Sigma)) for > 30 minutes. Slides were incubated in primary antibodies (listed below) in blocking solution overnight at 4°C. Slides were then washed three times with PBS +0.1% Tween 20 (Millipore Sigma) and subsequently incubated with secondary antibodies (listed below) for > 2 h at room temperature. Slides were then washed once more with PBS +0.1% Tween 20 prior to incubation in 1μM DAPI (Life Technologies) for 5 minutes, rinsed with PBS, and mounted with either Prolong Gold (Life Sciences) or Fluoroshield (Millipore Sigma). The following primary antibodies were used: rabbit anti-SPC (1:2000, Millipore Sigma), rat anti-RAGE (1:500, R&D Systems, clone 175410), rabbit anti-Krt5 (1:1000, BioLegend, clone Poly19055), chicken anti-Krt5 (1:500, BioLegend, clone Poly9059), goat anti-Scgb3a2 (1:200, R&D, clone AF3465), mouse anti-acetylated tubulin (1:2000, Millipore Sigma, clone 6-11B-1), rabbit anti-p63α (1:500, Cell Signaling, clone D2K8X), rabbit anti-ΔNp63 (1:100, BioLegend, clone Poly6190), and rat anti-Ki67 (1:1000, Thermo Fisher Scientific, clone SolA15). The following secondary antibodies were used: Alexa Fluor™ 488-conjugated donkey anti-rabbit (1:1000, Thermo Fisher Scientific), Alexa Fluor™ 488-conjugated donkey anti-rat (1:1000, Thermo Fisher Scientific), Alexa Fluor™ 488-conjugated donkey anti-goat (1:1000, Thermo Fisher Scientific), Alexa Fluor™ 488-conjugated donkey anti-chicken (1:500, Jackson Immuno Research), Alexa Fluor™ 647-conjugated donkey anti-rabbit (1:1000, Thermo Fisher Scientific), Alexa Fluor™ 647-conjugated donkey anti-rat (1:1000, Thermo Fisher Scientific), Alexa Fluor™ 647-conjugated donkey anti-goat (1:1000, Thermo Fisher Scientific), Alexa Fluor™ 647-conjugated donkey anti-chicken (1:500, Jackson Immuno Research), Alexa Fluor™ 488-conjugated donkey anti-mouse (1:500, Jackson Immuno Research), and Alexa Fluor™ 647-conjugated donkey anti-mouse (1:500, Thermo Fisher Scientific). The following conjugated antibodies were used: FITC-conjugated anti-mouse Ly6D (1:100, BioLegend, clone 49-H4). All protocols and primary, secondary, and conjugated antibodies were used for both mouse and human tissue.

Imaging—All images were taken on Leica DMi8 Microscope using a Leica DFC9000 sCMOS camera and Leica Application Suite X (LASX) software. Immunofluorescent and brightfield images were taken at either 10x, 20x, or 63x using the z stack and extended depth-of-field functions. Images were minimally processed prior to quantification or publication by adjusting the lookup table to lower the signal-to-noise ratio.

Immunofluorescent lineage tracing—For quantifying Sox2-traced cells in $Sox2^{\Delta Np63WT}$ and $Sox2^{\Delta Np63KO}$ mice, sections were cut and stained at three discrete levels

of the tissue block separated by at least 300μm each. In order to survey a large region of the lung and quantify as many airway/alveolar p63-trace^{+} expansion events as possible in p63$^{\Delta Np63WT}$ and p63$^{\Delta Np63KO}$ mice, we sampled twice the number of sections from each of three 300μm levels. Only sections containing either airway or alveolar p63-trace^{+} cells were stained and quantified. If no p63-trace^{+} cells in either location were found in a given level, a new level was cut and surveyed. Cell counting was performed in LASX software and copied to Microsoft Excel for further analysis.

Fluorescence-activated cell sorting—Lung cells were isolated by inflating lungs with 15 U/mL dispase II in HBSS (Thermo Fisher Scientific), tying off the trachea, and cutting lobes away from the mainstem bronchi. Lobes were then incubated in 15 U/mL dispase II for 45 min while shaking at room temperature and then mechanically dissociated by pipetting in sort buffer (SB; Dulbecco's modified Eagle's medium (DMEM) (Thermo Fisher Scientific) + 2% cosmic calf serum (CC; Thermo Fisher Scientific) + 1% P/S). After pelleting at 550 × g for 5 minutes at 4°C, whole-lung suspension was treated with Red Blood Cell Lysis Buffer (Millipore Sigma) for 5 minutes, pelleted, and resuspended in SB + 1:1000 DNase I (Millipore Sigma) for a 45-min recovery period shaking at 37°C. Whole-lung suspension was then repelleted and resuspended in SB + 1:50 TruStain FcX™ antibody (anti-mouse CD16/32, BioLegend) for a 10-min blocking period at 37°C. To sort post-flu intrapulmonary p63^{+} progenitors from Krt5^{CreERT2} mice, non-tamoxifen-treated Krt5$^{\Delta Np63WT}$ and Krt5$^{\Delta Np63KO}$ mice that lost ≥10% bodyweight were euthanized via isoflurane overdose at day 14 post-flu, had their lungs processed as above, and were stained with APC/Cy7-conjugated rat anti-mouse CD45 antibody (1:200, BioLegend, clone 30-F11), Alexa Fluor® 488-conjugated or PE/Cy7-conjugated rat anti-mouse CD326 (EpCAM) antibody (1:200, BioLegend, clone G8.8), Alexa Fluor® 647-conjugated rat anti-mouse CD104 (integrin β4) antibody (1:100, BioLegend, clone 346-11A), and FITC-conjugated rat anti-mouse Ly6D (1:100, BioLegend, clone 49-H4) for 45 minutes at 4°C, followed by a final spin-down at 550 × g for 5 minutes at 4°C. Stained cells and controls were then resuspended in SB + 1:1000 DNase + 1:1000 Draq7 (Beckman Coulter) as a live/dead stain. All FACS sorting was done on either a BD FACSJazz (BD Biosciences) or BD FACSAria (BD Biosciences) and cells were collected in round-bottom polystyrene tubes (Thermo Fisher Scientific) in 300μL DMEM + 20% CC + 2% P/S.

Primary intrapulmonary p63^{+} progenitor transplantation and quantification —Krt5$^{\Delta Np63HET}$ donors, Krt5$^{\Delta Np63KO}$ donors, and Krt5$^{CreERT2\ neg}$ recipient mice were infected with PR8 at the same time as in "influenza virus propagation and infection". Krt5$^{\Delta Np63HET}$ donors and Krt5$^{\Delta Np63KO}$ donors were given a single dose of 0.25mg/g IP tamoxifen at day 9 post-infection to induce lineage labelling but not fully recombine the ΔNp63^{flox} alleles (see results and Figures S4A–S4D). Three days later at day 12 post-infection, donor lungs were dissociated into single cells as in "fluorescence-activated cell sorting" and the bulk EpCAM^{+} integrin β4^{+} airway epithelial population containing Krt5-trace^{+} cells was isolated and resuspended in 30μL PBS + 1% P/S. Recipient mice were anesthetized with 3.5% isoflurane in 100% O_2 via an anesthesia vaporizer system and were intranasally administered cells by pipetting the single-cell suspension onto the nostrils of anesthetized mice in visually confirmed agonal breathing, as previously described.[92]

All recipient mice received at least 100k EpCAM$^+$ β4$^+$ cells at the time of transplant (on average 194k EpCAM$^+$ β4$^+$ cells were transplanted across all experiments). Transplanted cells were allowed to engraft for three days until day 15 post-infection, at which point recipient mice were administered IP tamoxifen every other day (on day 15, day 17, and day 19 post-infection/day 3, day 5, and day 7 post-transplant) for a total of three tamoxifen doses. One week following the final dose of tamoxifen at day 26 post-infection/day 14 post-transplant, recipient lungs were harvested as in "lung tissue preparation for immunostaining" and immunostained and imaged as in "immunostaining" and "imaging", respectively. Lobes with visible RFP$^+$ engraftments via whole-mount microscopy were separated and sectioned for lineage quantification. Slides were screened for engraftments via fluorescent microscopy as they were cut. To ensure that discrete cells within the engraftments were being quantified, only sections ≥14μm apart were co-stained with SPC and Krt5 and imaged.

Primary intrapulmonary p63$^+$ progenitor culture and passaging—Post-flu intrapulmonary p63$^+$ progenitors were isolated from non-tamoxifen-treated Krt5$^{\Delta Np63WT}$ and Krt5$^{\Delta Np63KO}$ mice by sorting live CD45$^-$ EpCAM$^+$ β4$^+$ Ly6D$^+$ cells from injured lungs at day 14 post-flu. Sorted intrapulmonary p63$^+$ progenitors were seeded onto 70μL of Matrigel (BD) in a 96-well clear polystyrene flat-bottom microplate (Millipore Sigma) to generate organoids. Media used for airway culture conditions was based on a modified dual SMAD inhibition media utilized for the long-term culture of basal epithelial cells[93] and allowed for intrapulmonary p63$^+$ progenitor growth as either organoids or monolayers, consisting of PneumaCult™-Ex Plus Medium (Stemcell Technologies) + 1x PneumaCult™-Ex Plus Supplement (Stemcell Technologies) + 1:1000 hydrocortisone stock solution (Stemcell Technologies) + 1μM A8301 (TGFb inhibitor, Millipore Sigma) + 10μM Y-27632 (ROCK inhibitor, Cayman Chemical) + 1:5000 Primocin® (Invivogen). Media used for alveolar culture conditions was based on conditions for primary mouse AT2 (C12)[92] and human iPSC-derived AT2 (CK+DCI)[72,73] culture. Briefly, CK+DCI was made according to[73] and supplemented with 50ng/mL EGF (Peprotech) + 200ng/mL Rspo1 (Peprotech) + 100ng/mL Noggin (Peprotech) + 100ng/mL FGF10 (Peprotech) + 1μM A8301 (TGFβ inhibitor) (Millipore Sigma) + 10μM Y-27632 (ROCK inhibitor) (Cayman Chemical). To passage organoids, organoids were treated with 15 U/mL dispase II in Hank's balanced salt solution (HBSS) for 30 minutes, rinsed with 2 mM EDTA (Thermo Fisher Scientific), incubated in 0.05% trypsin (Gibco) + 2 mM EDTA in PBS for 5 min at 37°C, mechanically dissociated by pipetting 50–100 times with a p200 pipette, quenched with DMEM + 10% CC + 1% P/S, and pelleted at 550 × g for 5 minutes at 4°C. Organoid seeding density for all experiments was 10k dissociated cells/96-well plate well. To passage monolayers, monolayers were treated with 0.05% trypsin (Gibco) + 2 mM EDTA in PBS for 10 min at 37°C, quenched with DMEM + 10% CC + 1% P/S, and pelleted at 550 × g for 5 minutes at 4°C.

Migration assay—Migration assays were performed using two-well silicone inserts (Ibidi). Upon securing a silicone insert on a culture plate, the surface within the insert was coated with 0.5% gelatin from bovine skin (Millipore Sigma) + 5% Matrigel (BD) for 15 min. Non-tamoxifentreated intrapulmonary p63$^+$ progenitors from Krt5$^{\Delta Np63KO}$ mice were previously adapted to monolayer conditions by passaging organoids and plating dissociated

cells on 0.5% gelatin from bovine skin +5% Matrigel for at least one passage as monolayers prior to seeding for the migration assay. 30k intrapulmonary $p63^+$ progenitors resuspended in airway media + 1μM 4OHT (Cayman Chemical) or an equivalent volume of DMSO were seeded on both sides of the silicone insert and allowed to form monolayers for 48 h. After 48 h, the insert was removed and images were taken immediately for the 0h time point. Images were also taken at 6h and 24h following insert removal. 10x magnification brightfield images were taken at each time point. Three discreet regions of the gap were imaged at each time point for each replicate of each condition (−4OHT (vehicle only) and +4OHT). All experiments were performed in technical triplicate with cells derived from the same original donor mouse between passages 8 and 10. Images in TIFF format were exported from LASX to FIJI. After setting the image scale, the "Polygon selection" tool was used to trace the gap and measured using the "Analyze - > Set Measurements - > Area" function in FIJI for all regions imaged for each replicate for each condition. We derived the migration rate by subtracting the area at 6h after insert removal from the area at 0h after insert removal from that same replicate and dividing by the time elapsed (6 h) for each replicate for each condition (ex. (0h area – 6h area)/6).

Cytospins—Cells were isolated according to "Primary intrapulmonary $p63^+$ progenitor culture and passaging" and pelleted at 550 × *g* for 5 minutes at 4°C before resuspension in 200μL 3.2% PFA per number of slides to be cytospun. 200μL of resuspended cells were loaded into cytospin chambers and spun at 750 rpm for 5 minutes on a Cytospin 2 (Shandon).

Monolayer and organoid bulk RNA-sequencing culture experiments—For monolayer bulk RNA-sequencing experiments, post-flu intrapulmonary $p63^+$ progenitors from a non-tamoxifen-treated $Krt5^{\Delta Np63KO}$ mouse were expanded as organoids in airway media and adapted to monolayer conditions as in "migration assay and quantification". Monolayers were maintained in airway media for these experiments. Technical triplicates for the −4OHT and +4OHT groups were expanded in parallel. DMSO or 1μM 4OHT was added to the media for all triplicates when they reached ~80% confluence and was maintained in the media for 48 h. Monolayer cells were harvested for RNA using the monolayer passaging method in "Primary intrapulmonary $p63^+$ progenitor culture and passaging", pelleted at 550 × g for 5 minutes at 4°C, and stored directly at −80°C until RNA extraction. For organoid bulk RNA-sequencing experiments, post-flu intrapulmonary $p63^+$ progenitors from a non-tamoxifen-treated $Krt5^{\Delta Np63KO}$ mouse were first expanded as organoids in airway media seeded on top of 70μL Matrigel. Organoids were then passaged using the organoid passaging method in "Primary intrapulmonary $p63^+$ progenitor culture and passaging" and seeded in 50μL Matrigel droplets at a seeding density of 250 cell/μL Matrigel. After allowing the droplets to solidify at 37°C for 15 min, airway or alveolar media (without DMSO or 4OHT) was added to the droplets and the seeded cells were allowed to form organoids in their respective media conditions for 24 h. At 24 h post-plating, media was changed to airway media + 1μM 4OHT or an equivalent volume of DMSO or alveolar media + 1μM 4OHT or an equivalent volume of DMSO. Organoids were maintained in these conditions for seven days and harvested for RNA using the organoid passaging method in "Primary

intrapulmonary p63^{+} progenitor culture and passaging", pelleted at 550 × g for 5 minutes at 4°C, and stored directly at −80°C until RNA extraction.

RNA isolation and qPCR—For bulk RNA-sequencing experiments, RNA was isolated using the ReliaPrep™ RNA Cell Miniprep kit (Promega). For injury time course qPCR of ΔNp63 expression, ≥300 live CD45^{-} EpCAM^{+} β4^{+} p63-trace^{+} cells were sorted at each indicated time point directly into Takara SMART-Seq HT Kit (Takara) 1x reaction buffer on ice and amplified for 20 cycles. A 1:20 dilution of amplified cDNA in deionized water was used as input in each qPCR reaction well. Gene expression was calculated relative to *Rpl19* ("L19") within that sample and expressed as fold change over the average expression. qPCR was run on an Applied Biosystems QuantStudio 6 Real-Time PCR System (Thermo Fisher Scientific) with PowerUp SYBR Green Master Mix (Applied Biosystems). All primer sets are as listed in Table S2.

Bulk RNA-sequencing analysis—For monolayer, airway organoid, and alveolar organoid bulk sequencing, three technical replicates treated as described in "monolayer and organoid bulk RNA-sequencing culture experiments" were sequenced for each treatment group (three replicates each for both ΔNp63WT and ΔNp63KO cells in all conditions). RNA was extracted from all samples as in "rna isolation and qpcr" and shipped overnight on dry ice to Genewiz for library preparation and sequencing. PolyA-selected RNA was used to generate libraries using the NEBNext Ultra II RNA Library Prep Kit for Illumina (NEB) according to the manufacturer's instructions. Sequencing was performed using a 2 × 150bp paired-end configuration on an Illumnia HiSeq at a read depth of ~45 million reads per sample on average. Reads were aligned to the mm10 mouse genome using Kallisto and imported into R Studio for analysis via the TxImport package. Transcripts with low counts were filtered out if they had 1) zero reads in any sample, or 2) less than at least one count per million in at least two samples. Data was then normalized using the trimmed mean of M values normalization method[94] in the EdgeR package. Mean-variance trend fitting, linear modeling, and Bayesian statistics for differential gene expression analysis were performed using the Voom, LmFit, and eBayes functions, respectively, of the Limma package, yielding differentially expressed genes between ΔNp63WT and ΔNp63KO groups.

ChIP and ChIP-sequencing—Monolayers for ChIP-sequencing were treated exactly in parallel with monolayer bulk RNA-sequencing experiments. Two 10cm plates of ~90% confluent DMSO-treated post-flu intrapulmonary p63^{+} progenitors from a non-tamoxifen-treated Krt5$^{\Delta Np63KO}$ mouse grown in airway media were harvested for each of three p63 ChIP technical replicates. One 10cm plate of ~90% confluent either DMSO- or 1μM 4OHT-treated post-flu intrapulmonary p63^{+} progenitors from a non-tamoxifen-treated Krt5$^{\Delta Np63KO}$ mouse grown in airway media was harvested for each of three ΔNp63WT and ΔNp63KO technical replicates for both H3K27ac and H3K27me3 ChIP. ChIP sample processing was followed according to the SimpleChIP® Plus Enzymatic Chromatic IP with Magnetic Beads Kit (Cell Signaling) protocol. In short, after 48h in either DMSO or 1μM 4OHT, media was removed and monolayers were cross-linked for 20 min in 1% PFA. Following fixation quenching with glycine and pelleting, nuclei were isolated, treated with micrococcal nuclease, and sonicated four times for 15 s each with an ultrasonic sonicator with a 1/8-

inch probe on ice to shear chromatin into 150bp-900bp fragments. 5ug of cross-linked, digested chromatin was immunoprecipitated using 1ug of either rabbit anti-p63α (Cell Signaling, clone D2K8X), rabbit anti-H3K27ac (Cell Signaling, clone D5E4), or rabbit anti-H3K27me3 (Cell Signaling, clone C36B11). 2% inputs samples were generated for all replicates of each immunoprecipitation, and given nine ΔNp63WT ChIP samples and six ΔNp63KO ChIP samples in total, 1/9 of each ΔNp63WT 2% input were combined and 1/6 of each ΔNp63KO 2% input were combined a to generate a universal ΔNp63WT 2% input sample and universal ΔNp63KO 2% input sample, respectively. Eluted ChIP DNA was used to generate libraries using the NEBNext® Ultra™ II DNA Library Prep Kit for Illumina (NEB) according to the manufacturer's instructions. After library cleanup, library concentrations were quantified using a Qubit 2.0 Fluorometer (Thermo Fisher Scientific) and size validated on a TapeStation (Agilent Technologies). Prepared libraries were sent to Genewiz for sequencing. Sequencing was performed using a 2 × 150bp paired-end configuration on an Illumnia® HiSeq at a read depth of ~27 million reads per sample on average.

Organoid histology—For organoid histology, dissociated monolayer cells were seeded inside a 50μL Matrigel droplet on a 6-well clear polystyrene flat-bottom plate (Millipore Sigma) at a density of 250 cell/μL Matrigel in the indicated media conditions + 1μM 4OHT or an equivalent volume of DMSO at the time of seeding. After culture for one week in these conditions, droplets were incubated in 1x TBS for 10 min, fixed with IHC Zinc Fixative (BD Biosciences) for 30 min, incubated in 30% sucrose in TBS shaking overnight at 4°C, and incubated for two hours in 15% sucrose in TBS +50% OCT compound at room temperature. Finally, the fixed organoid-containing Matrigel droplets were scraped from plate with a weighing spatula and randomly oriented and embedded in OCT by flash freezing with dry ice and ethanol. Sectioning and immunostaining were performed as described in "Immunostaining".

QUANTIFICATION AND STATISTICAL ANALYSIS

Pulse oximetry analysis—Each data point for one-year SpO_2 timelines represents the average SpO_2 for each individual mouse at the given time point. n = 5 uninfected young mice, n = 3 uninfected one-year-old mice, and n = 4 infected mice whose SpO_2 was repeatedly measured at both eight months and one-year post-infection. Significance based on one-way ANOVA. For $Sox2^{CreERT2}$-mediated ΔNp63 knockout SpO_2, $Sox2^{\Delta Np63WT}$ n = 5 mice and $Sox2^{\Delta Np63KO}$ n = 5 mice. For $p63^{CreERT2}$-mediated ΔNp63 knockout SpO_2, $p63^{\Delta Np63WT}$ n = 7 mice and $p63^{\Delta Np63KO}$ n = 5 mice. Each data point for $Sox2^{CreERT2}$-mediated ΔNp63 knockout and $p63^{CreERT2}$-mediated ΔNp63 knockout SpO_2 timelines represents the average SpO_2 across all mice for a given group. Significance based on ordinary two-way ANOVA performed in GraphPad Prism 7. Data represented as mean ± standard error. *p < 0.05, **p < 0.01, ***p < 0.001, ****p < 0.0001 for all statistics.

Immunofluorescent lineage tracing quantification—For IAV-Cre tracing quantification, n = 3 IAV-Cre infected mice quantified at each time point. For $Sox2^{CreERT2}$-mediated ΔNp63 knockout quantification, $Sox2^{\Delta Np63WT}$ n = 3 mice and $Sox2^{\Delta Np63KO}$ n = 3 mice. For $p63^{CreERT2}$-mediated ΔNp63 knockout quantification, $p63^{\Delta Np63WT}$ n = 3

mice and p63$^{\Delta Np63KO}$ n = 5 mice. For all lineage tracing quantification graphs, each data point represents the average number of ≥500 cells across R3 levels bearing each lineage marker from an individual mouse for the corresponding experiment. Two-way ANOVA and unpaired Welch's t-tests were performed for these analyses in GraphPad Prism 7. Data represented as mean ± standard deviation and *p < 0.05, **p < 0.01, ***p < 0.001, ****p < 0.0001 for all statistics.

Orthotopic transplantation quantification—For orthotopic transplantation quantification, an average of 683 Krt5-trace^{+} engrafted cells were quantified for SPC and Krt5 expression across all experiments. n = 2 recipient lungs of Krt5$^{\Delta Np63HET}$ donor cells from different donor mice analyzed and n = 2 recipient lungs of Krt5$^{\Delta Np63KO}$ donor cells from different donor mice analyzed. Significance based on unpaired Welch's t test. Data represented as mean ± standard deviation and *p < 0.05, **p < 0.01, ***p < 0.001, ****p < 0.0001 for all statistics.

Migration assay quantification—For migration assay quantification and graphs, ΔNp63WT n = 3 technical replicates and ΔNp63KO n = 3 technical replicates. Significance based on two-way ANOVA for gap closure analysis and unpaired Welch's t test for migratory rate analysis. Data represented as mean ± standard deviation and *p < 0.05, **p < 0.01, ***p < 0.001, ****p < 0.0001 for all statistics.

Cytospin quantification—Following the cytospin protocol as described in "cytospins", ≥ 100 cells were counted across ≥ 20x fields of view from independent sorts to collect Ly6D^{+} cells from n = 3 different wild-type mice.

Bulk RNA-sequencing analysis—ΔNp63WT n = 3 technical replicates and ΔNp63KO n = 3 technical replicates for monolayer, airway organoid, and alveolar organoid sequencing experiments. Z scores for heatmap generation were calculated using FPKM values and significantly differentially expressed genes were called based on adjusted p value < 0.05.

ChIP-sequencing analysis and motif enrichment—For p63 ChIP-sequencing, n = 3 ΔNp63WT technical replicates were used. For H3K27ac and H3K27me3 ChIP-sequencing, n = 3 ΔNp63WT technical replicates and n = 3 ΔNp63KO technical replicates were used. Following "ChIP-sequencing and motif enrichment", FASTQ files were uploaded to usegalaxy.org[95] for processing. Adapter sequences were trimmed and quality checked using Trim Galore! followed by Bowtie2 alignment to the built-in mm10 mouse genome index. Trimmed and aligned files were processed using Samtools so that only properly mapped, paired, non-duplicate, non-mitochondrial, non-blacklisted reads remained. Based on PCA analyses, a single H3K27me3 among the ΔNp63KO samples was a clear outlier (likely due to poor immunoprecipitation) and was removed from subsequent analysis. MACS2[96] was used for peak calling of p63, H3K27ac, and H3K27me3 ChIP with corresponding universal 2% input controls for reference. For p63 and H3K27ac ChIP, peak calling was performed with default MACS2 settings and an FDR <0.05. Due to difficulty in calling H3K27me3 peaks in ΔNp63KO samples, a stringent p value cutoff of <0.01 rather than FDR was used to identify peaks in H3K27me3 ChIP samples. Analyses downstream of MACS2 peak calling were performed in a combination of R Studio and usegalaxy.org. Peak annotation

and heatmap generation based on MACS2 outputs was performed using the ChIPseeker package.[97] Differential enrichment analysis was also performed on MACS2 outputs using the DiffBind package,[98] which identified 13,733 differentially enriched H3K27ac regions and 5838 differentially enriched H3K27me3 regions. The GenomicRanges package[99] was used to convert DiffBind differentially enriched regions into Granges objects to annotate enrichment to nearby genes using ChIPseeker. Granges objects were also used with the ChIPpeakAnno package[100] to identify overlapping p63 and H3K27ac or H3K27me3 ChIP regions. MEME-ChIP[101,102] was used for motif discovery and motif enrichment analysis of up to the top 2000 peaks (or all 2004 peaks in the case of p63 ChIP) for all differentially enriched regions. Samtools was used to merge BAM files for all replicates of each condition and loaded into IGV for ChIP coverage and peak visualization.

Human single cell sequencing analysis—The annotated full-size RDS file from the single cell sequencing dataset[50] from healthy and IPF patients was downloaded from the Gene Expression Omnibus (GEO) under the accession code GEO: GSE135893. In R Studio using the Seurat library, cells from the clusters annotated “Basal” and “KRT5−/KRT17+” were subsetted out with the donor’s health status and TP63 expression and saved in CSV format. In Microsoft Excel, TP63 expression of the cells from each donor extracted in this way was averaged and stratified based on health status. No additional analyses, re-clustering, or ad hoc processing was performed on the downloaded dataset to perform this analysis. Each data point represents the average TP63 expression of all cells for a given donor, with n = 9 healthy donors and n = 20 IPF donors for cells whose average TP63 expression was measured in the “Basal” cluster and n = 2 healthy donors and n = 16 IPF donors whose average TP63 expression was measured in the “KRT5−/KRT17+” cluster. One-way ANOVA was performed for these analyses in GraphPad Prism 7. Data represented as mean ± standard deviation and *$p < 0.05$, **$p < 0.01$, ***$p < 0.001$, ****$p < 0.0001$ for all statistics.

Statistics—Data was collected in Microsoft Excel and imported into GraphPad Prism 7 to generate all graphs and perform all statistical testing. Details of statistical test used, sample size, and definition of significance can be found in corresponding figure legends and the “quantification and statistical analysis” section of the STAR Methods.

Supplementary Material

Refer to Web version on PubMed Central for supplementary material.

ACKNOWLEDGMENTS

The authors appreciate all past and present Vaughan lab members for engaging discussions and creating a cordial and stimulating environment in which to perform this work, and undergraduate student Marcella Soewignjo for image quantification. We thank the Penn Lung Biology Institute Human Lung Tissue Bank, UCSF Interstitial Lung Disease Blood and Tissue Repository, and CHOP Flow Cytometry Core for their assistance in performing these studies. We also thank Dr. Montserrat Anguera and Dr. Isabel Sierra for their invaluable insight into designing, performing, and analyzing the ChIP-seq experiments, recommendations on epigenetics bioinformatics tools, and generosity with reagents. We are grateful to Dr. Andres Blanco, Dr. Christopher Lengner, Dr. Lisa Young, Dr. Edward Morrisey, and Dr. Panteleimon Rompolas for serving on the dissertation committee for which this work was the primary thesis. We thank Dr. Noam Cohen for facilitating additional access to flow sorters, members of the Morrisey lab for intellectual discussion, and BioRender for providing a platform to create the cartoons and schematics used in figures throughout this report. This work was supported by NIH grants

R01HL153539, R01HL164350, and a grant from the Lisa Dean Moseley Foundation to A.E.V. and an NIH grant 1F31HL15259701A1 to A.I.W.

INCLUSION AND DIVERSITY

One or more of the authors of this paper self-identifies as a gender minority in their field of research. One or more of the authors of this paper self-identifies as a member of the LGBTQIA+ community. One or more of the authors of this paper self-identifies as an underrepresented ethnic minority in their field of research or within their geographical location. One or more of the authors of this paper received support from a program designed to increase minority representation in their field of research.

REFERENCES

1. Evans MJ, Cabral LJ, Stephens RJ, and Freeman G (1973). Renewal of alveolar epithelium in the rat following exposure to NO2. Am. J. Pathol. 70, 175–198. [PubMed: 4566990]
2. Kim CFB, Jackson EL, Woolfenden AE, Lawrence S, Babar I, Vogel S, Crowley D, Bronson RT, and Jacks T (2005). Identification of bronchioalveolar stem cells in normal lung and lung cancer. Cell 121, 823–835. 10.1016/j.cell.2005.03.032. [PubMed: 15960971]
3. Barkauskas CE, Cronce MJ, Rackley CR, Bowie EJ, Keene DR, Stripp BR, Randell SH, Noble PW, and Hogan BLM (2013). Type 2 alveolar cells are stem cells in adult lung. J. Clin. Invest. 123, 3025–3036. [PubMed: 23921127]
4. Liu Q, Liu K, Cui G, Huang X, Yao S, Guo W, Qin Z, Li Y, Yang R, Pu W, et al. (2019). Lung regeneration by multipotent stem cells residing at the bronchioalveolar-duct junction. Nat. Genet. 51, 728–738. 10.1038/s41588-019-0346-6. [PubMed: 30778223]
5. Kathiriya JJ, Brumwell AN, Jackson JR, Tang X, and Chapman HA (2020). Distinct airway epithelial stem cells hide among club cells but mobilize to promote alveolar regeneration. Cell Stem Cell 26, 346–358.e4. 10.1016/j.stem.2019.12.014. [PubMed: 31978363]
6. Vaughan AE, Brumwell AN, Xi Y, Gotts JE, Brownfield DG, Treutlein B, Tan K, Tan V, Liu FC, Looney MR, et al. (2015). Line-age-negative progenitors mobilize to regenerate lung epithelium after major injury. Nature 517, 621–625. 10.1038/nature14112. [PubMed: 25533958]
7. Kanegai CM, Xi Y, Donne ML, Gotts JE, Driver IH, Amidzic G, Lechner AJ, Jones KD, Vaughan AE, Chapman HA, and Rock JR (2016). Persistent pathology in influenza-infected mouse lungs. Am. J. Respir. Cell Mol. Biol. 55, 613–615. [PubMed: 27689795]
8. Seibold MA, Smith RW, Urbanek C, Groshong SD, Cosgrove GP, Brown KK, Schwarz MI, Schwartz DA, and Reynolds SD (2013). The idiopathic pulmonary fibrosis honeycomb cyst contains a mucocilary pseudostratified epithelium. PLoS One 8, e58658. 10.1371/journal.pone.0058658. [PubMed: 23527003]
9. Smirnova NF, Schamberger AC, Nayakanti S, Hatz R, Behr J, and Eickelberg O (2016). Detection and quantification of epithelial progenitor cell populations in human healthy and IPF lungs. Respir. Res. 17, 83. 10.1186/s12931-016-0404-x. [PubMed: 27423691]
10. Taylor MS, Chivukula RR, Myers LC, Jeck WR, Waghray A, Tata PR, Selig MK, O'Donnell WJ, Farver CF, Thompson BT, et al. (2018). A conserved distal lung regenerative pathway in acute lung injury. Am. J. Pathol. 188, 1149–1160. 10.1016/j.ajpath.2018.01.021. [PubMed: 29476724]
11. Zhao Z, Zhao Y, Zhou Y, Wang X, Zhang T, and Zuo W (2020). Single-cell analysis identified lung progenitor cells in COVID-19 patients. Cell Prolif 53, e12931. 10.1111/cpr.12931. [PubMed: 33094537]
12. M. Fernanda de Mello Costa, A.I. Weiner, and A.E. Vaughan (2020). Basal-like progenitor cells: a review of dysplastic alveolar regeneration and remodeling in lung repair. Stem Cell Rep. 15, 1015–1025. 10.1016/j.stemcr.2020.09.006.
13. Melms JC, Biermann J, Huang H, Wang Y, Nair A, Tagore S, Katsyv I, Rendeiro AF, Amin AD, Schapiro D, et al. (2021). A molecular single-cell lung atlas of lethal COVID-19. Nature 595, 114–119. 10.1038/s41586-021-03569-1. [PubMed: 33915568]

14. Liu W, Peng L, Liu H, and Hua S (2015). Pulmonary function and clinical manifestations of patients infected with mild influenza A virus subtype H1N1: a one-year follow-up. PLoS One 10, e0133698. 10.1371/journal.pone.0133698. [PubMed: 26218647]
15. Koppe S, Túlio AIB, Villegas ILP, and Motter AA (2016). Pulmonary function in patients with pandemic H1N1. Mov. Out. 29, 805–812.
16. Wang F, Kream RM, and Stefano GB (2020). Long-term respiratory and neurological sequelae of COVID-19. Med. Sci. Monit. 26, e928996. 10.12659/MSM.928996. [PubMed: 33177481]
17. Desai AD, Lavelle M, Boursiquot BC, and Wan EY (2022). Long-term complications of COVID-19. Am. J. Physiol. Cell Physiol. 322, C1–C11. 10.1152/ajpcell.00375.2021. [PubMed: 34817268]
18. Compagnone N, Palumbo D, Cremona G, Vitali G, De Lorenzo R, Calvi MR, Del Prete A, Baiardo Redaelli M, S. Calamarà, A. Belletti, et al. (2022). Residual lung damage following ARDS in COVID-19 ICU survivors. Acta Anaesthesiol. Scand. 66, 223–231. 10.1111/aas.13996. [PubMed: 34758108]
19. Yang Y, Riccio P, Schotsaert M, Mori M, Lu J, Lee DK, García-Sastre A, Xu J, and Cardoso WV (2018). Spatial-temporal lineage restrictions of embryonic p63(+) progenitors establish distinct stem cell pools in adult airways. Dev. Cell 44, 752–761.e4. 10.1016/j.devcel.2018.03.001. [PubMed: 29587145]
20. Quantius J, Schmoldt C, Vazquez-Armendariz AI, Becker C, El Agha E, Wilhelm J, Morty RE, Vadász I, Mayer K, Gattenloehner S, et al. (2016). Influenza virus infects epithelial stem/progenitor cells of the distal lung: impact on Fgfr2b-driven epithelial repair. PLoS Pathog. 12. e1005544. [PubMed: 27322618]
21. Xi Y, Kim T, Brumwell AN, Driver IH, Wei Y, Tan V, Jackson JR, Xu J, Lee DK, Gotts JE, et al. (2017). Local lung hypoxia determines epithelial fate decisions during alveolar regeneration. Nat. Cell Biol. 19, 904–914. 10.1038/ncb3580. [PubMed: 28737769]
22. Yuan T, Volckaert T, Redente EF, Hopkins S, Klinkhammer K, Wasnick R, Chao CM, Yuan J, Zhang JS, Yao C, et al. (2019). FGF10-FGFR2B signaling generates basal cells and drives alveolar epithelial regeneration by bronchial epithelial stem cells after lung injury. Stem Cell Rep. 12, 1041–1055. 10.1016/j.stemcr.2019.04.003.
23. Pellegrini G, Dellambra E, Golisano O, Martinelli E, Fantozzi I, Bondanza S, Ponzin D, McKeon F, and De Luca M (2001). p63 identifies keratinocyte stem cells. Proc. Natl. Acad. Sci. USA 98, 3156–3161. 10.1073/pnas.061032098. [PubMed: 11248048]
24. Signoretti S, Waltregny D, Dilks J, Isaac B, Lin D, Garraway L, Yang A, Montironi R, McKeon F, and Loda M (2000). p63 is a prostate basal cell marker and is required for prostate development. Am. J. Pathol. 157, 1769–1775. 10.1016/S0002-9440(10)64814-6. [PubMed: 11106548]
25. Signoretti S, Pires MM, Lindauer M, Horner JW, Grisanzio C, Dhar S, Majumder P, McKeon F, Kantoff PW, Sellers WR, and Loda M (2005). p63 regulates commitment to the prostate cell lineage. Proc. Natl. Acad. Sci. USA 102, 11355–11360. 10.1073/pnas.0500165102. [PubMed: 16051706]
26. Barbareschi M, Pecciarini L, Cangi MG, Macrì E, Rizzo A, Viale G, and Doglioni C (2001). p63, a p53 homologue, is a selective nuclear marker of myoepithelial cells of the human breast. Am. J. Surg. Pathol. 25, 1054–1060. [PubMed: 11474290]
27. Van Keymeulen A, Rocha AS, Ousset M, Beck B, Bouvencourt G, Rock J, Sharma N, Dekoninck S, and Blanpain C (2011). Distinct stem cells contribute to mammary gland development and maintenance. Nature 479, 189–193. 10.1038/nature10573. [PubMed: 21983963]
28. Rock JR, Onaitis MW, Rawlins EL, Lu Y, Clark CP, Xue Y, Randell SH, and Hogan BLM (2009). Basal cells as stem cells of the mouse trachea and human airway epithelium. Proc. Natl. Acad. Sci. USA 106, 12771–12775. 10.1073/pnas.0906850106. [PubMed: 19625615]
29. Romano RA, Smalley K, Magraw C, Serna VA, Kurita T, Raghavan S, and Sinha S (2012). DeltaNp63 knockout mice reveal its indispensable role as a master regulator of epithelial development and differentiation. Development 139, 772–782. 10.1242/dev.071191. [PubMed: 22274697]

30. Yang A, Schweitzer R, Sun D, Kaghad M, Walker N, Bronson RT, Tabin C, Sharpe A, Caput D, Crum C, and McKeon F (1999). p63 is essential for regenerative proliferation in limb, craniofacial and epithelial development. Nature 398, 714–718. 10.1038/19539. [PubMed: 10227294]

31. Truong AB, Kretz M, Ridky TW, Kimmel R, and Khavari PA (2006). p63 regulates proliferation and differentiation of developmentally mature keratinocytes. Genes Dev. 20, 3185–3197. 10.1101/gad.1463206. [PubMed: 17114587]

32. Carroll DK, Carroll JS, Leong CO, Cheng F, Brown M, Mills AA, Brugge JS, and Ellisen LW (2006). p63 regulates an adhesion programme and cell survival in epithelial cells. Nat. Cell Biol. 8, 551–561. 10.1038/ncb1420. [PubMed: 16715076]

33. Gu X, Coates PJ, Boldrup L, and Nylander K (2008). p63 contributes to cell invasion and migration in squamous cell carcinoma of the head and neck. Cancer Lett. 263, 26–34. 10.1016/j.canlet.2007.12.011. [PubMed: 18194839]

34. Giacobbe A, Compagnone M, Bongiorno-Borbone L, Antonov A, Markert EK, Zhou JH, Annicchiarico-Petruzzelli M, Melino G, and Peschiaroli A (2016). p63 controls cell migration and invasion by transcriptional regulation of MTSS1. Oncogene 35, 1602–1608. 10.1038/onc.2015.230. [PubMed: 26119942]

35. Kouwenhoven EN, Oti M, Niehues H, van Heeringen SJ, Schalkwijk J, Stunnenberg HG, van Bokhoven H, and Zhou H (2015). Transcription factor p63 bookmarks and regulates dynamic enhancers during epidermal differentiation. EMBO Rep. 16, 863–878. 10.15252/embr.201439941. [PubMed: 26034101]

36. Haas M, Gómez Vázquez JL, Sun DI, Tran HT, Brislinger M, Tasca A, Shomroni O, Vleminckx K, and Walentek P (2019). DeltaN-Tp63 mediates Wnt/beta-Catenin-induced inhibition of differentiation in basal stem cells of mucociliary epithelia. Cell Rep. 28, 3338–3352.e6. 10.1016/j.celrep.2019.08.063. [PubMed: 31553905]

37. Kurata SI, Okuyama T, Osada M, Watanabe T, Tomimori Y, Sato S, Iwai A, Tsuji T, Ikawa Y, and Katoh I (2004). p51/p63 Controls subunit alpha3 of the major epidermis integrin anchoring the stem cells to the niche. J. Biol. Chem. 279, 50069–50077. 10.1074/jbc.M406322200. [PubMed: 15361520]

38. Ihrie RA, Marques MR, Nguyen BT, Horner JS, Papazoglu C, Bronson RT, Mills AA, and Attardi LD (2005). Perp is a p63-regulated gene essential for epithelial integrity. Cell 120, 843–856. 10.1016/j.cell.2005.01.008. [PubMed: 15797384]

39. Laurikkala J, Mikkola ML, James M, Tummers M, Mills AA, and Thesleff I (2006). p63 regulates multiple signalling pathways required for ectodermal organogenesis and differentiation. Development 133, 1553–1563. 10.1242/dev.02325. [PubMed: 16524929]

40. Romano RA, Ortt K, Birkaya B, Smalley K, and Sinha S (2009). An active role of the DeltaN isoform of p63 in regulating basal keratin genes K5 and K14 and directing epidermal cell fate. PLoS One 4, e5623. 10.1371/journal.pone.0005623. [PubMed: 19461998]

41. Ferone G, Mollo MR, Thomason HA, Antonini D, Zhou H, Ambrosio R, De Rosa L, Salvatore D, Getsios S, van Bokhoven H, et al. (2013). p63 control of desmosome gene expression and adhesion is compromised in AEC syndrome. Hum. Mol. Genet. 22, 531–543. 10.1093/hmg/dds464. [PubMed: 23108156]

42. Fessing MY, Mardaryev AN, Gdula MR, Sharov AA, Sharova TY, Rapisarda V, Gordon KB, Smorodchenko AD, Poterlowicz K, Ferone G, et al. (2011). p63 regulates Satb1 to control tissue-specific chromatin remodeling during development of the epidermis. J. Cell Biol. 194, 825–839. 10.1083/jcb.201101148. [PubMed: 21930775]

43. Mardaryev AN, Gdula MR, Yarker JL, Emelianov VU, Emelianov VN, Poterlowicz K, Sharov AA, Sharova TY, Scarpa JA, Joffe B, et al. (2014). p63 and Brg1 control developmentally regulated higher-order chromatin remodelling at the epidermal differentiation complex locus in epidermal progenitor cells. Development 141, 101–111. 10.1242/dev.103200. [PubMed: 24346698]

44. Sethi I, Sinha S, and Buck MJ (2014). Role of chromatin and transcriptional co-regulators in mediating p63-genome interactions in keratinocytes. BMC Genom. 15, 1042. 10.1186/1471-2164-15-1042.

45. Fan X, Wang D, Burgmaier JE, Teng Y, Romano RA, Sinha S, and Yi R (2018). Single cell and open chromatin analysis reveals molecular origin of epidermal cells of the skin. Dev. Cell 47, 133. 10.1016/j.devcel.2018.09.019. [PubMed: 30300587]

46. Qu J, Yi G, and Zhou H (2019). p63 cooperates with CTCF to modulate chromatin architecture in skin keratinocytes. Epigenet. Chromatin 12, 31. 10.1186/s13072-019-0280-y.
47. Lin-Shiao E, Lan Y, Welzenbach J, Alexander KA, Zhang Z, Knapp M, Mangold E, Sammons M, Ludwig KU, and Berger SL (2019). p63 establishes epithelial enhancers at critical craniofacial development genes. Sci. Adv. 5, eaaw0946. 10.1126/sciadv.aaw0946. [PubMed: 31049400]
48. Santos-Pereira JM, Gallardo-Fuentes L, Neto A, Acemel RD, and Tena JJ (2019). Pioneer and repressive functions of p63 during zebrafish embryonic ectoderm specification. Nat. Commun. 10, 3049. 10.1038/s41467-019-11121-z. [PubMed: 31296872]
49. Yu X, Singh PK, Tabrejee S, Sinha S, and Buck MJ (2021). DeltaNp63 is a pioneer factor that binds inaccessible chromatin and elicits chromatin remodeling. Epigenet. Chromatin 14, 20. 10.1186/s13072-021-00394-8.
50. Habermann AC, Gutierrez AJ, Bui LT, Yahn SL, Winters NI, Calvi CL, Peter L, Chung MI, Taylor CJ, Jetter C, et al. (2020). Single-cell RNA sequencing reveals profibrotic roles of distinct epithelial and mesenchymal lineages in pulmonary fibrosis. Sci. Adv. 6, eaba1972. 10.1126/sciadv.aba1972. [PubMed: 32832598]
51. Neumark N, Cosme C Jr., Rose K-A, and Kaminski N (2020). The idiopathic pulmonary fibrosis cell atlas. Am. J. Physiol. Lung Cell Mol. Physiol. 319, L887–L893. [PubMed: 32996785]
52. Heaton NS, Langlois RA, Sachs D, Lim JK, Palese P, and tenOever BR (2014). Long-term survival of influenza virus infected club cells drives immunopathology. J. Exp. Med. 211, 1707–1714. 10.1084/jem.20140488. [PubMed: 25135297]
53. Hamilton JR, Sachs D, Lim JK, Langlois RA, Palese P, and Heaton NS (2016). Club cells surviving influenza A virus infection induce temporary nonspecific antiviral immunity. Proc. Natl. Acad. Sci. USA 113, 3861–3866. 10.1073/pnas.1522376113. [PubMed: 27001854]
54. Strunz M, Simon LM, Ansari M, Kathiriya JJ, Angelidis I, Mayr CH, Tsidiridis G, Lange M, Mattner LF, Yee M, et al. (2020). Alveolar regeneration through a Krt8+ transitional stem cell state that persists in human lung fibrosis. Nat. Commun. 11, 3559. 10.1038/s41467-020-17358-3. [PubMed: 32678092]
55. Choi J, Park JE, Tsagkogeorga G, Yanagita M, Koo BK, Han N, and Lee JH (2020). Inflammatory signals induce AT2 cell-derived damage-associated transient progenitors that mediate alveolar regeneration. Cell Stem Cell 27, 366–382.e7. 10.1016/j.stem.2020.06.020. [PubMed: 32750316]
56. Kobayashi Y, Tata A, Konkimalla A, Katsura H, Lee RF, Ou J, Banovich NE, Kropski JA, and Tata PR (2020). Persistence of a regeneration-associated, transitional alveolar epithelial cell state in pulmonary fibrosis. Nat. Cell Biol. 22, 934–946. 10.1038/s41556-020-0542-8. [PubMed: 32661339]
57. Kathiriya JJ, Wang C, Zhou M, Brumwell A, Cassandras M, Le Saux CJ, Cohen M, Alysandratos KD, Wang B, Wolters P, et al. (2022). Human alveolar type 2 epithelium transdifferentiates into metaplastic KRT5(+) basal cells. Nat. Cell Biol. 24, 10–23. 10.1038/s41556-021-00809-4. [PubMed: 34969962]
58. Ray S, Chiba N, Yao C, Guan X, McConnell AM, Brockway B, Que L, McQualter JL, and Stripp BR (2016). Rare SOX2+ airway progenitor cells generate KRT5+ cells that repopulate damaged alveolar parenchyma following influenza virus infection. Stem Cell Rep. 7, 817–825.
59. Madisen L, Zwingman TA, Sunkin SM, Oh SW, Zariwala HA, Gu H, Ng LL, Palmiter RD, Hawrylycz MJ, Jones AR, et al. (2010). A robust and high-throughput Cre reporting and characterization system for the whole mouse brain. Nat. Neurosci. 13, 133–140. 10.1038/nn.2467. [PubMed: 20023653]
60. Arnold K, Sarkar A, Yram MA, Polo JM, Bronson R, Sengupta S, Seandel M, Geijsen N, and Hochedlinger K (2011). Sox2(+) adult stem and progenitor cells are important for tissue regeneration and survival of mice. Cell Stem Cell 9, 317–329. 10.1016/j.stem.2011.09.001. [PubMed: 21982232]
61. Chakravarti D, Su X, Cho MS, Bui NHB, Coarfa C, Venkatanarayan A, Benham AL, Flores González RE, Alana J, Xiao W, et al. (2014). Induced multipotency in adult keratinocytes through down-regulation of DeltaNp63 or DGCR8. Proc. Natl. Acad. Sci. USA 111, E572–E581. 10.1073/pnas.1319743111. [PubMed: 24449888]

62. Rawlins EL, Okubo T, Xue Y, Brass DM, Auten RL, Hasegawa H, Wang F, and Hogan BLM (2009). The role of Scgb1a1+ Clara cells in the long-term maintenance and repair of lung airway, but not alveolar, epithelium. Cell Stem Cell 4, 525–534. 10.1016/j.stem.2009.04.002. [PubMed: 19497281]

63. Kumar PA, Hu Y, Yamamoto Y, Hoe NB, Wei TS, Mu D, Sun Y, Joo LS, Dagher R, Zielonka EM, et al. (2011). Distal airway stem cells yield alveoli in vitro and during lung regeneration following H1N1 influenza infection. Cell 147, 525–538. [PubMed: 22036562]

64. Candi E, Rufini A, Terrinoni A, Dinsdale D, Ranalli M, Paradisi A, De Laurenzi V, Spagnoli LG, Catani MV, Ramadan S, et al. (2006). Differential roles of p63 isoforms in epidermal development: selective genetic complementation in p63 null mice. Cell Death Differ. 13, 1037–1047. 10.1038/sj.cdd.4401926. [PubMed: 16601749]

65. Chapman HA, Li X, Alexander JP, Brumwell A, Lorizio W, Tan K, Sonnenberg A, Wei Y, and Vu TH (2011). Integrin alpha6beta4 identifies an adult distal lung epithelial population with regenerative potential in mice. J. Clin. Invest. 121, 2855–2862. 10.1172/JCI57673. [PubMed: 21701069]

66. Chakrabarti R, Wei Y, Hwang J, Hang X, Andres Blanco M, Choudhury A, Tiede B, Romano RA, DeCoste C, Mercatali L, et al. (2014). DeltaNp63 promotes stem cell activity in mammary gland development and basal-like breast cancer by enhancing Fzd7 expression and Wnt signalling. Nat. Cell Biol. 16, 1004–1015.1–13. 10.1038/ncb3040. [PubMed: 25241036]

67. Qu J, Tanis SEJ, Smits JPH, Kouwenhoven EN, Oti M, van den Bogaard EH, Logie C, Stunnenberg HG, van Bokhoven H, Mulder KW, and Zhou H (2018). Mutant p63 affects epidermal cell identity through rewiring the enhancer landscape. Cell Rep. 25, 3490–3503.e4. 10.1016/j.celrep.2018.11.039. [PubMed: 30566872]

68. Kaufman CK, Sinha S, Bolotin D, Fan J, and Fuchs E (2002). Dissection of a complex enhancer element: maintenance of keratinocyte specificity but loss of differentiation specificity. Mol. Cell Biol. 22, 4293–4308. 10.1128/MCB.22.12.4293-4308.2002. [PubMed: 12024040]

69. Kiyokawa H, Yamaoka A, Matsuoka C, Tokuhara T, Abe T, and Morimoto M (2021). Airway basal stem cells reutilize the embryonic proliferation regulator, Tgfbeta-Id2 axis, for tissue regeneration. Dev. Cell 56, 1917–1929.e9. 10.1016/j.devcel.2021.05.016. [PubMed: 34129836]

70. Liberti DC, Liberti Iii WA, Kremp MM, Penkala IJ, Cardenas-Diaz FL, Morley MP, Babu A, Zhou S, Fernandez Iii RJ, and Morrisey EE (2022). Klf5 defines alveolar epithelial type 1 cell lineage commitment during lung development and regeneration. Dev. Cell 57, 1742–1757.e5. 10.1016/j.devcel.2022.06.007. [PubMed: 35803279]

71. Vaughan AE, and Chapman HA (2013). Regenerative activity of the lung after epithelial injury. Biochim. Biophys. Acta 1832, 922–930. 10.1016/j.bbadis.2012.11.020. [PubMed: 23219956]

72. Jacob A, Morley M, Hawkins F, McCauley KB, Jean JC, Heins H, Na CL, Weaver TE, Vedaie M, Hurley K, et al. (2017). Differentiation of human pluripotent stem cells into functional lung alveolar epithelial cells. Cell Stem Cell 21, 472–488.e10. 10.1016/j.stem.2017.08.014. [PubMed: 28965766]

73. Jacob A, Vedaie M, Roberts DA, Thomas DC, Villacorta-Martin C, Alysandratos KD, Hawkins F, and Kotton DN (2019). Derivation of self-renewing lung alveolar epithelial type II cells from human pluripotent stem cells. Nat. Protoc. 14, 3303–3332. 10.1038/s41596-019-0220-0. [PubMed: 31732721]

74. Salwig I, Spitznagel B, Vazquez-Armendariz AI, Khalooghi K, Guenther S, Herold S, Szibor M, and Braun T (2019). Bronchioalveolar stem cells are a main source for regeneration of distal lung epithelia in vivo. EMBO J. 38, e102099. 10.15252/embj.2019102099. [PubMed: 31028085]

75. Tata PR, Mou H, Pardo-Saganta A, Zhao R, Prabhu M, Law BM, Vinarsky V, Cho JL, Breton S, Sahay A, et al. (2013). Dedifferentiation of committed epithelial cells into stem cells in vivo. Nature 503, 218–223. 10.1038/nature12777. [PubMed: 24196716]

76. Zuo W, Zhang T, Wu DZ, Guan SP, Liew AA, Yamamoto Y, Wang X, Lim SJ, Vincent M, Lessard M, et al. (2015). p63(+) Krt5(+) distal airway stem cells are essential for lung regeneration. Nature 517, 616–620. 10.1038/nature13903. [PubMed: 25383540]

77. Jiang M, Li H, Zhang Y, Yang Y, Lu R, Liu K, Lin S, Lan X, Wang H, Wu H, et al. (2017). Transitional basal cells at the squamous-columnar junction generate Barrett's oesophagus. Nature 550, 529–533. 10.1038/nature24269. [PubMed: 29019984]

78. Blanco MA, Sykes DB, Gu L, Wu M, Petroni R, Karnik R, Wawer M, Rico J, Li H, Jacobus WD, et al. (2021). Chromatin-state barriers enforce an irreversible mammalian cell fate decision. Cell Rep. 37, 109967. 10.1016/j.celrep.2021.109967. [PubMed: 34758323]

79. Stergachis AB, Haugen E, Shafer A, Fu W, Vernot B, Reynolds A, Raubitschek A, Ziegler S, LeProust EM, Akey JM, and Stamatoyannopoulos JA (2013). Exonic transcription factor binding directs codon choice and affects protein evolution. Science 342, 1367–1372. 10.1126/science.1243490. [PubMed: 24337295]

80. Fiszbein A, Krick KS, Begg BE, and Burge CB (2019). Exon-mediated activation of transcription starts. Cell 179, 1551–1565.e17. 10.1016/j.cell.2019.11.002. [PubMed: 31787377]

81. Ritter DI, Dong Z, Guo S, and Chuang JH (2012). Transcriptional enhancers in protein-coding exons of vertebrate developmental genes. PLoS One 7, e35202. 10.1371/journal.pone.0035202. [PubMed: 22567096]

82. Birnbaum RY, Clowney EJ, Agamy O, Kim MJ, Zhao J, Yamanaka T, Pappalardo Z, Clarke SL, Wenger AM, Nguyen L, et al. (2012). Coding exons function as tissue-specific enhancers of nearby genes. Genome Res. 22, 1059–1068. 10.1101/gr.133546.111. [PubMed: 22442009]

83. Ramsey MR, He L, Forster N, Ory B, and Ellisen LW (2011). Physical association of HDAC1 and HDAC2 with p63 mediates transcriptional repression and tumor maintenance in squamous cell carcinoma. Cancer Res. 71, 4373–4379. 10.1158/0008-5472.CAN-11-0046. [PubMed: 21527555]

84. Yin Z, Gonzales L, Kolla V, Rath N, Zhang Y, Lu MM, Kimura S, Ballard PL, Beers MF, Epstein JA, and Morrisey EE (2006). Hop functions downstream of Nkx2.1 and GATA6 to mediate HDAC-dependent negative regulation of pulmonary gene expression. Am. J. Physiol. Lung Cell Mol. Physiol. 291, L191–L199. 10.1152/ajplung.00385.2005. [PubMed: 16510470]

85. Zhou B, Zhong Q, Minoo P, Li C, Ann DK, Frenkel B, Morrisey EE, Crandall ED, and Borok Z (2008). Foxp2 inhibits Nkx2.1-mediated transcription of SP-C via interactions with the Nkx2.1 homeodomain. Am. J. Respir. Cell Mol. Biol. 38, 750–758. 10.1165/rcmb.2007-0350OC. [PubMed: 18239190]

86. Cheung WKC, Zhao M, Liu Z, Stevens LE, Cao PD, Fang JE, Westbrook TF, and Nguyen DX (2013). Control of alveolar differentiation by the lineage transcription factors GATA6 and HOPX inhibits lung adenocarcinoma metastasis. Cancer Cell 23, 725–738. 10.1016/j.ccr.2013.04.009. [PubMed: 23707782]

87. Little DR, Gerner-Mauro KN, Flodby P, Crandall ED, Borok Z, Akiyama H, Kimura S, Ostrin EJ, and Chen J (2019). Transcriptional control of lung alveolar type 1 cell development and maintenance by NK homeobox 2–1. Proc. Natl. Acad. Sci. USA 116, 20545–20555. 10.1073/pnas.1906663116. [PubMed: 31548395]

88. Little DR, Lynch AM, Yan Y, Akiyama H, Kimura S, and Chen J (2021). Differential chromatin binding of the lung lineage transcription factor NKX2–1 resolves opposing murine alveolar cell fates in vivo. Nat. Commun. 12, 2509. 10.1038/s41467-021-22817-6. [PubMed: 33947861]

89. Su X, Paris M, Gi YJ, Tsai KY, Cho MS, Lin YL, Biernaskie JA, Sinha S, Prives C, Pevny LH, et al. (2009). TAp63 prevents premature aging by promoting adult stem cell maintenance. Cell Stem Cell 5, 64–75. 10.1016/j.stem.2009.04.003. [PubMed: 19570515]

90. Lee DK, Liu Y, Liao L, Wang F, and Xu J (2014). The prostate basal cell (BC) heterogeneity and the p63-positive BC differentiation spectrum in mice. Int. J. Biol. Sci. 10, 1007–1017. 10.7150/ijbs.9997. [PubMed: 25210499]

91. Xue J, Chambers BS, Hensley SE, and López CB (2016). Propagation and characterization of influenza virus stocks that lack high levels of defective viral genomes and hemagglutinin mutations. Front. Microbiol. 7, 326. 10.3389/fmicb.2016.00326. [PubMed: 27047455]

92. Weiner AI, Jackson SR, Zhao G, Quansah KK, Farshchian JN, Neupauer KM, Littauer EQ, Paris AJ, Liberti DC, Scott Worthen G, et al. (2019). Mesenchyme-free expansion and transplantation of adult alveolar progenitor cells: steps toward cell-based regenerative therapies. NPJ Regen. Med. 4, 17.

93. Mou H, Vinarsky V, Tata PR, Brazauskas K, Choi SH, Crooke AK, Zhang B, Solomon GM, Turner B, Bihler H, et al. (2016). Dual SMAD signaling inhibition enables long-term expansion of diverse epithelial basal cells. Cell Stem Cell 19, 217–231. 10.1016/j.stem.2016.05.012. [PubMed: 27320041]

94. Robinson MD, and Oshlack A (2010). A scaling normalization method for differential expression analysis of RNA-seq data. Genome Biol. 11, R25. 10.1186/gb-2010-11-3-r25. [PubMed: 20196867]

95. Afgan E, Nekrutenko A, Grüning BA, Blankenberg D, Goecks J, Schatz MC, Ostrovsky AE, Mahmoud A, Lonie AJ, Syme A, et al. (2022). The Galaxy platform for accessible, reproducible and collaborative biomedical analyses: 2022 update. Nucleic Acids Res. 50, W345–W351. 10.1093/nar/gkac247. [PubMed: 35446428]

96. Zhang Y, Liu T, Meyer CA, Eeckhoute J, Johnson DS, Bernstein BE, Nusbaum C, Myers RM, Brown M, Li W, and Liu XS (2008). Model-based analysis of ChIP-seq (MACS). Genome Biol. 9, R137. 10.1186/gb-2008-9-9-r137. [PubMed: 18798982]

97. Yu G, Wang LG, and He QY (2015). ChIPseeker: an R/Bioconductor package for ChIP peak annotation, comparison and visualization. Bioinformatics 31, 2382–2383. 10.1093/bioinformatics/btv145. [PubMed: 25765347]

98. Ross-Innes CS, Stark R, Teschendorff AE, Holmes KA, Ali HR, Dunning MJ, Brown GD, Gojis O, Ellis IO, Green AR, et al. (2012). Differential oestrogen receptor binding is associated with clinical outcome in breast cancer. Nature 481, 389–393. 10.1038/nature10730. [PubMed: 22217937]

99. Lawrence M, Huber W, Pagès H, Aboyoun P, Carlson M, Gentleman R, Morgan MT, and Carey VJ (2013). Software for computing and annotating genomic ranges. PLoS Comput. Biol. 9, e1003118. 10.1371/journal.pcbi.1003118. [PubMed: 23950696]

100. Zhu LJ, Gazin C, Lawson ND, H. Pagè s, S.M. Lin, D.S. Lapointe, and M.R. Green (2010). ChIPpeakAnno: a bioconductor package to annotate ChIP-seq and ChIP-chip data. BMC Bioinf. 11, 237. 10.1186/1471-2105-11-237.

101. Bailey TL, Boden M, Buske FA, Frith M, Grant CE, Clementi L, Ren J, Li WW, and Noble WS (2009). Meme suite: tools for motif discovery and searching. Nucleic Acids Res. 37, W202–W208. 10.1093/nar/gkp335. [PubMed: 19458158]

102. Bailey TL, Johnson J, Grant CE, and Noble WS (2015). The MEME suite. Nucleic Acids Res. 43, W39–W49. 10.1093/nar/gkv416. [PubMed: 25953851]

Highlights

- ΔNp63 is necessary for dysplastic alveolar remodeling
- Injured mice without dysplasia exhibit enhanced functional recovery
- ΔNp63 restricts plasticity by maintaining chromatin modifications at distinct loci
- Basal cells undergo differentiation dependent upon niche cues and ΔNp63 loss

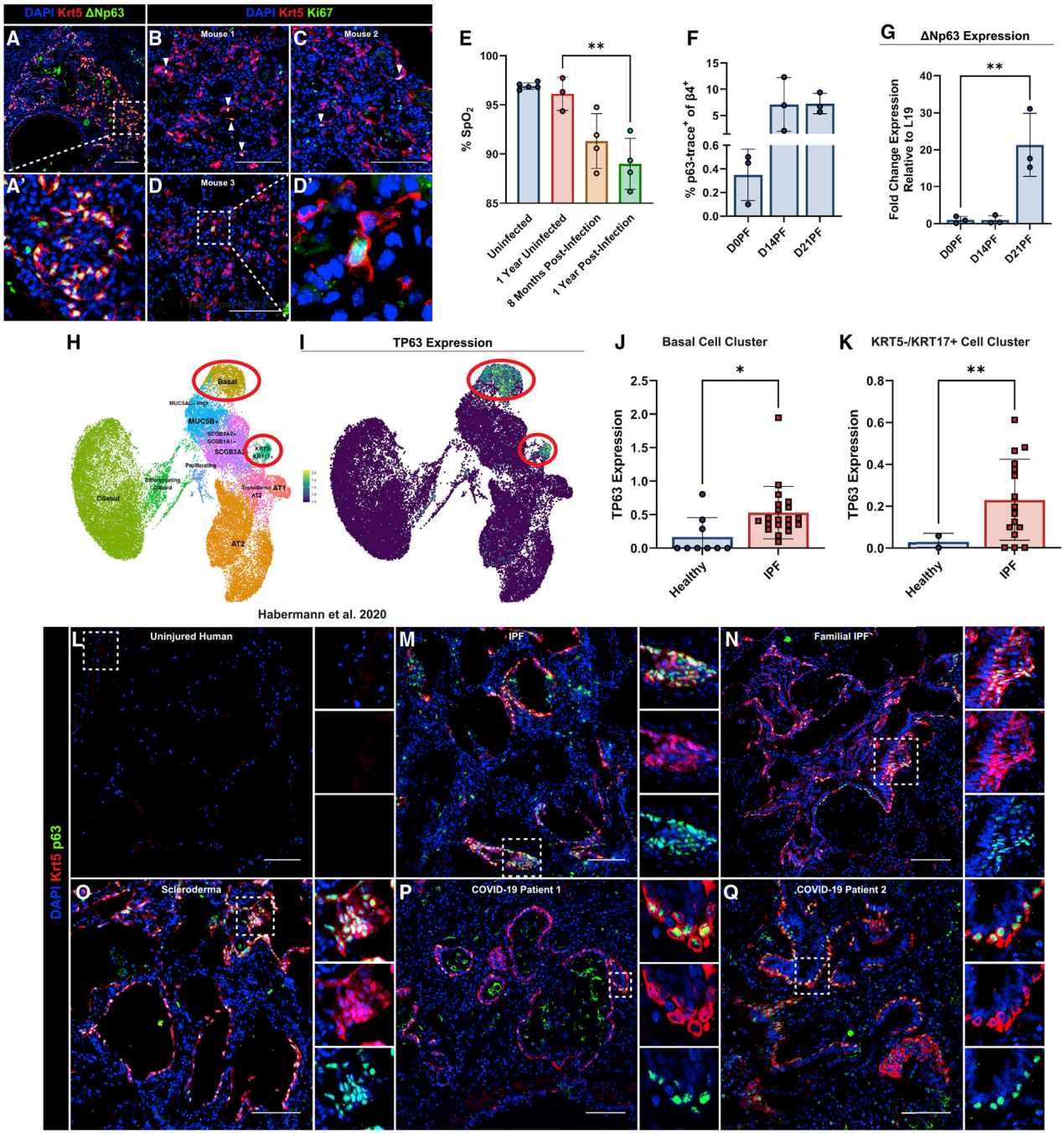

Figure 1. Dysplastic alveolar remodeling persists long-term in injured mice and humans and is correlated with ΔNp63 expression

(A) ΔNp63^{+} Krt5^{+} dysplastic remodeling persists in murine alveolar regions 1 year post flu. Scale bars, = 100μm. (A′) Inset of outlined region in (A).

(B–D) Representative images of Krt5^{+} Ki67^{+} proliferating dysplastic cells (white arrows) from three mice (100% of mice surveyed). Scale bars, 100μm. (D′) 63× magnification inset image of outlined region in (D).

(E) Pulse oximetry readings were taken on uninjured 2- to 3-month-old mice, uninjured 1-year-old mice, injured mice at 8 months post infection, and the samemice at 1 year post infection. Significance based on ordinary one-way ANOVA.

(F) Flow cytometry quantification during injury time course of percent p63-trace^{+} as a fraction of live CD45^{-} EpCAM^{+} β4^{+} cells.

(G) ΔNp63 expression increases in sorted p63-trace^{+} cells with injury progression. Significance based on ordinary one-way ANOVA.

(H) Human healthy and IPF epithelial cell uniform manifold approximation and projection from IPF Cell Atlas[50,51] with basal and KRT5^{-}/KRT17^{+} clusters highlighted.

(I) TP63 expression is largely restricted to basal and KRT5^{-}/KRT17^{+} clusters in cells from both healthy and IPF patients from IPF Cell Atlas.[50,51]

(J and K) TP63 expression is significantly upregulated in IPF patient epithelial cells compared with healthy epithelial cells from both the (J) basal and (K) KRT5^{-}/KRT17^{+} clusters. Significance for both (J) and (K) based on Welch's t test.

(L–Q) Representative immunofluorescence staining for Krt5 and p63 in alveolar regions of (L) uninjured human, (M) IPF patient, (N) familial IPF patient, (O) scleroderma patient, and (P and Q) two COVID-19 patient lungs. Krt5^{+} p63^{+} dysplastic pods are only found in injured alveoli. Insets are of outlined regions. Scale bars, 100μm.

Data presented as mean ± standard deviation with *p < 0.05, **p < 0.01, ***p < 0.001, ****p < 0.0001 for all statistics.

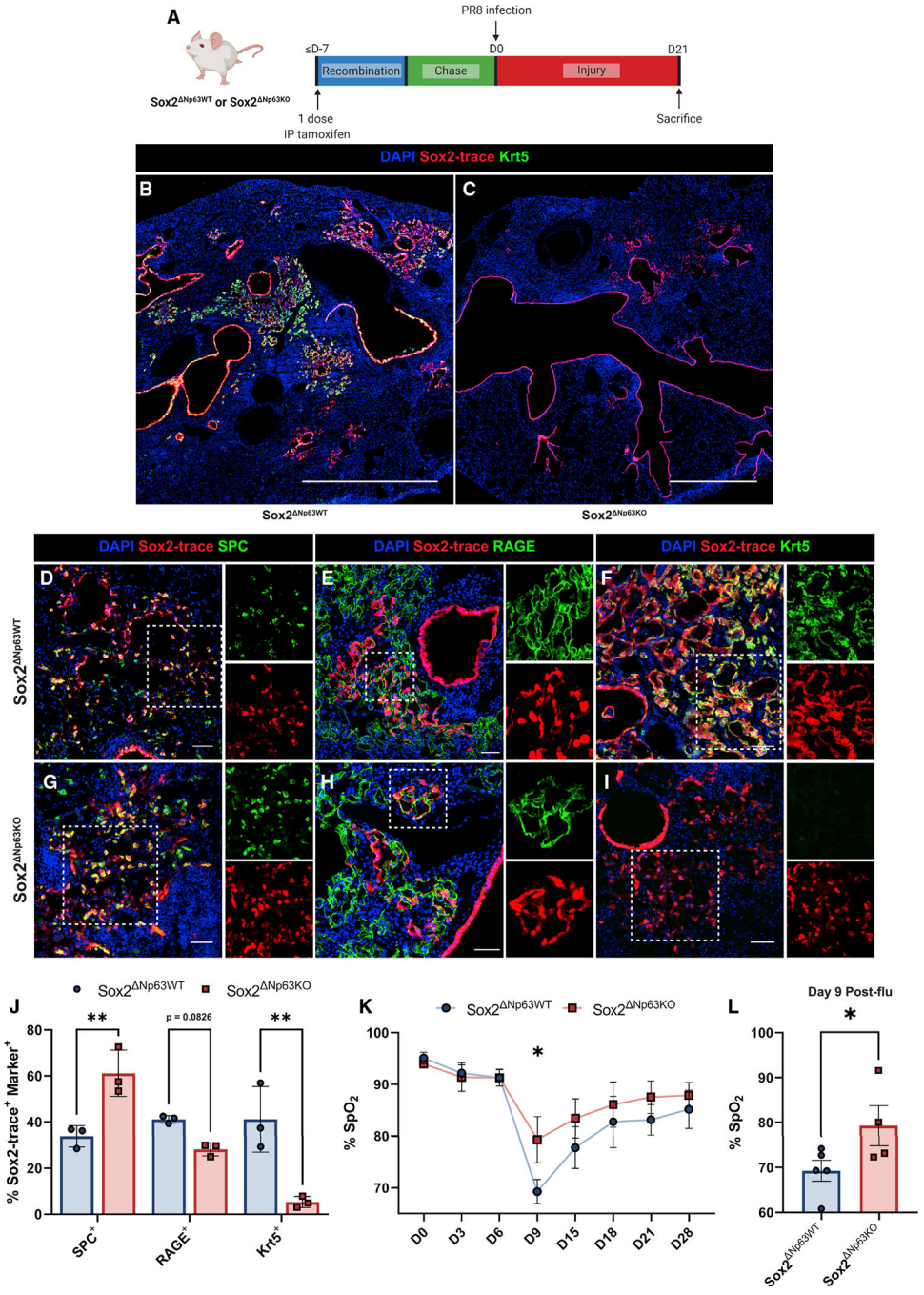

Figure 2. ΔNp63 is required for airway epithelial contribution to dysplastic remodeling *in vivo*

(A) Experimental timeline of Sox2-mediated ΔNp63 deletion.

(B) 20× tilescan of a $Sox2^{\Delta Np63WT}$ lobe shows normal Sox2-trace$^+$ contribution to alveolar repair, including Krt5$^+$ dysplasia. Scale bar, 1 mm.

(C) $Sox2^{\Delta Np63KO}$ lungs bear no Krt5$^+$ dysplastic areas. Scale bar, 1 mm.

(D–I) Representative images of alveolar Sox2-trace overlap with lineage markers. $Sox2^{\Delta Np63WT}$ mice exhibit expansion of (D) Sox2-trace$^+$ SPC$^+$ AT2s, (E) Sox2-trace$^+$ RAGE$^+$ AT1s, and (F) Sox2-trace$^+$ Krt5$^+$ dysplastic cells, whereas $Sox2^{\Delta Np63KO}$ mice have

only (G) Sox2-trace^{+} SPC^{+} AT2s and (H) Sox2-trace^{+} RAGE^{+} AT1s but lack (I) Sox2-trace^{+} Krt5^{+} dysplastic cells. Insets are of outlined regions. Scale bars, 50 μm.

(J) Quantification of Sox2-trace contribution to SPC^{+} AT2s, RAGE^{+} AT1s, and Krt5^{+} dysplasia.

(K) Pulse oximetry readings taken of injured Sox2$^{\Delta Np63WT}$ and Sox2$^{\Delta Np63KO}$ mice over a 4-week injury time course.

(L) Significantly higher blood oxygen saturation was detected at day 9 post flu in Sox2$^{\Delta Np63KO}$ mice.

Significance in (J–L) based on ordinary two-way ANOVA. Data in (J) presented as mean ± standard deviation and mean ± standard error in (K) and (L). *$p < 0.05$, **$p < 0.01$, ***$p < 0.001$, ****$p < 0.0001$ for all statistics.

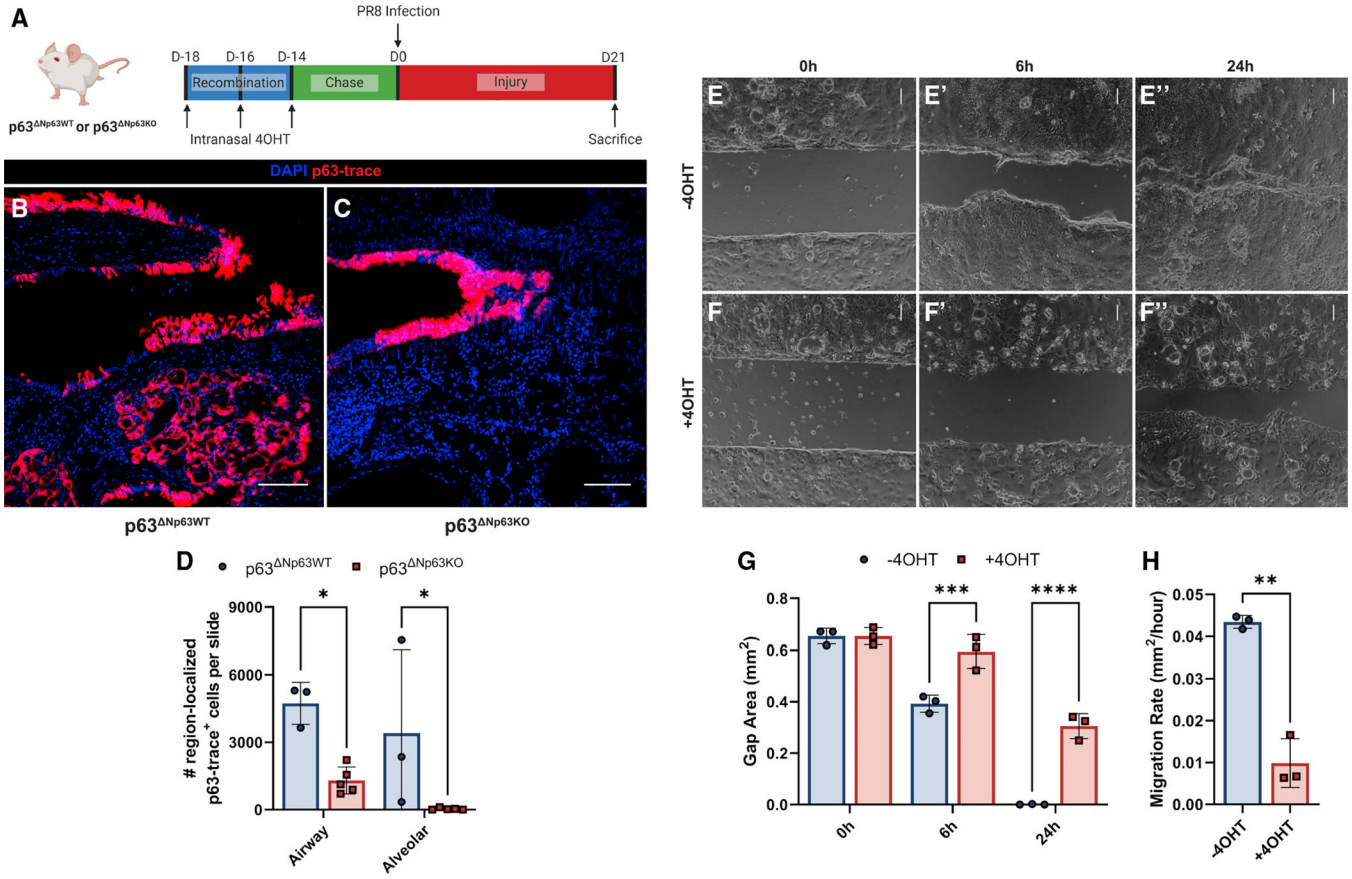

Figure 3. ΔNp63^{KO} intrapulmonary p63^{+} progenitors fail to migrate from airways *in vivo*

(A) Experimental timeline of p63-mediated ΔNp63 deletion.

(B) p63-trace^{+} cells contribute to both airway and alveolar repair in p63$^{\Delta Np63WT}$ mice. Scale bar, 100 μm.

(C) p63-trace^{+} cells do not contribute to alveolar repair in p63$^{\Delta Np63KO}$ mice, remaining only in the airways. Scale bar, 100 μm.

(D) Quantification of p63-trace^{+} cells in either the airways or alveoli in p63$^{\Delta Np63WT}$ or p63$^{\Delta Np63KO}$ mice. Significance based on mixed-effects analysis.

(E and F″) Brightfield images of migration assay at (E and F) 0 h, (E′ and F′) 6 h, and (E″ and F″) 24 h time points. Scale bars, 100 μm.

(G) Quantification of gap-area closure from migration experiment shows that while DMSO/−4OHT-treated monolayers can close the gap by 24 h post insert removal, +4OHT-treated (ΔNp63^{KO}) monolayers do not fully close the gap. Significance based on ordinary two-way ANOVA.

(H) Comparison of area migration rate in mm^2/h, revealing that +4OHT-treated (ΔNp63^{KO}) intrapulmonary p63^{+} progenitors migrate ~4 times slower than −4OHT (vehicle)-treated (ΔNp63^{WT}) intrapulmonary p63^{+} progenitors.

Significance based on Welch's t test. Data presented as mean ± standard deviation with *p < 0.05, **p < 0.01, ***p < 0.001, ****p < 0.0001 for all statistics.

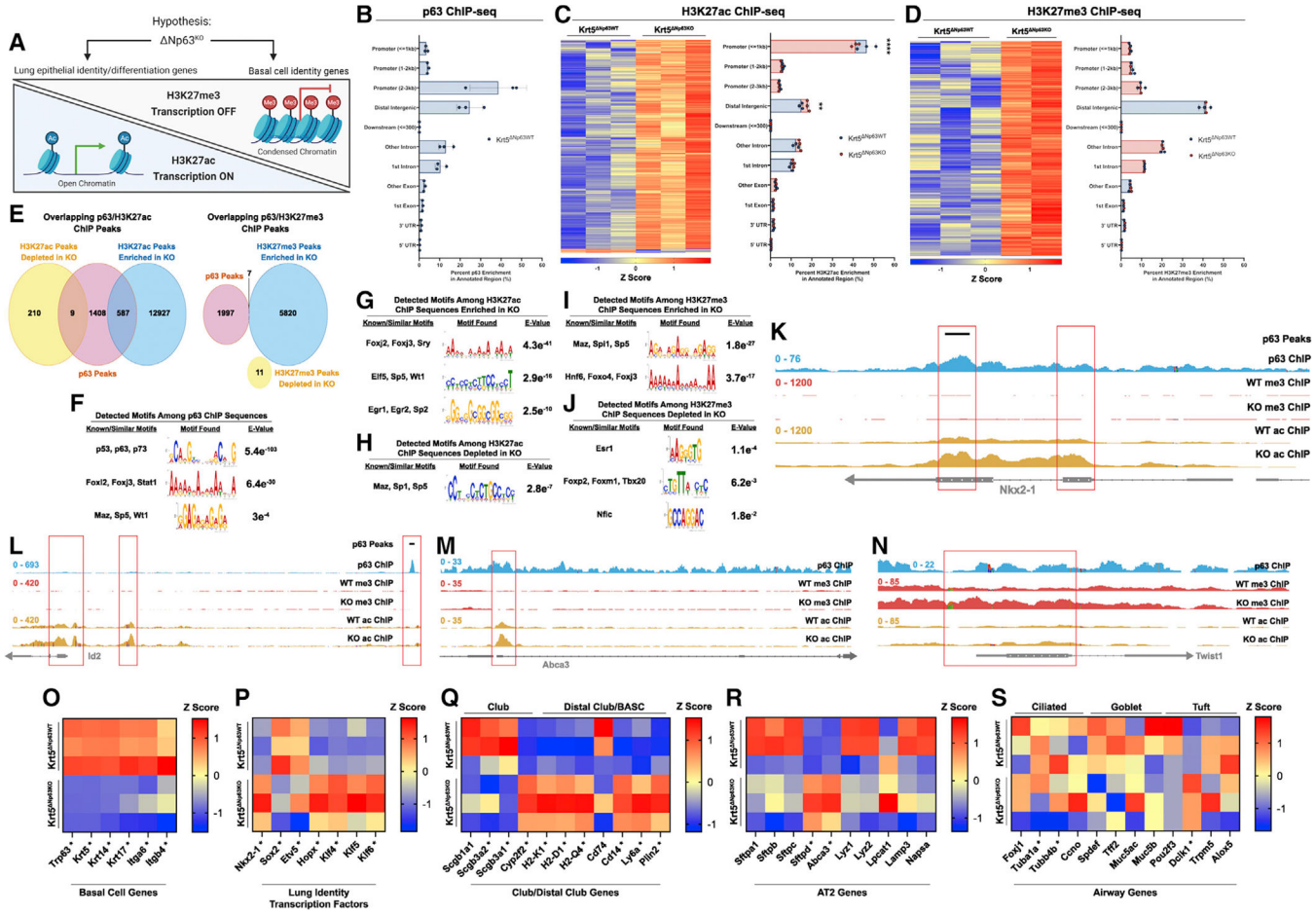

Figure 4. Intrapulmonary p63^{+} progenitor transcriptional and epigenetic states are regulated by ΔNp63

(A) Schematic of ChIP-seq experiment hypothesis.

(B) Genomic feature annotation for p63 peaks.

(C) Heatmap of differentially enriched/depleted H3K27ac peaks (left) and genomic feature annotation for H3K27ac Krt5$^{\Delta Np63WT}$ versus Krt5$^{\Delta Np63KO}$ peaks (right). Differentially enriched regions based on Krt5$^{\Delta Np63WT}$ (n = 3) and Krt5$^{\Delta Np63KO}$ (n = 3) with false discovery rate (FDR) <0.05.

(D) Heatmap of differentially enriched/depleted H3K27me3 peaks (left) and genomic feature annotation for H3K27me3 Krt5$^{\Delta Np63WT}$ versus Krt5$^{\Delta Np63KO}$ peaks (right). Differentially enriched regions based on Krt5$^{\Delta Np63WT}$ (n = 3) and Krt5$^{\Delta Np63KO}$ (n = 2) with p value <0.01.

(E) Overlap of p63 peaks with enriched/depleted H3K27ac peaks (left) and of p63 peaks with enriched/depleted H3K27me3 peaks (right).

(F) MEME-ChIP *de novo* motif discovery from p63-immunoprecipitated sequences.

(G–J) MEME-ChIP *de novo* motif discovery from (G) H3K27ac-immunoprecipitated sequences enriched in Krt5$^{\Delta Np63KO}$, (H) H3K27ac-immunoprecipitated sequences depleted in Krt5$^{\Delta Np63KO}$, (I) H3K27me3-immunoprecipitated sequences enriched in Krt5$^{\Delta Np63KO}$, and (J) H3K27me3-immunoprecipitated sequences depleted in Krt5$^{\Delta Np63KO}$.

(K–N) ChIP coverage tracks of p63, H3K27ac, and H3K27me3 from Krt5$^{\Delta Np63WT}$ and Krt5$^{\Delta Np63KO}$ monolayers show enrichment of H3K27ac at alveolar differentiation genes in including (K) Nkx2–1, (L) Id2, and (M) Abca3, along with enrichment of H3K27me3 at the EMT regulator (N) Twist1 following ΔNp63^{KO}. p63 ChIP peak calling identified an exonic p63 binding site in exon 2 of Nkx2–1, representing the most differentially H3K27ac enriched region at the Nkx2–1 locus following loss of ΔNp63. Red boxes are used to highlight regions of interest with called p63 binding sites and/or changes in histone modification enrichment.

(O–S) Heatmaps from bulk RNA-seq of ΔNp63^{WT} and ΔNp63^{KO} monolayers. Alterations in histone modifications correlate with changes in transcriptional identity upon ΔNp63 deletion, focusing on (O) basal cell markers, (P) lung identity transcription factors, (Q) club and distal club/BASC markers, (R) AT2 markers, and (S) differentiated airway epithelial cell markers. Genes marked with an asterisk are significantly differentially expressed with adjusted p value of <0.05.

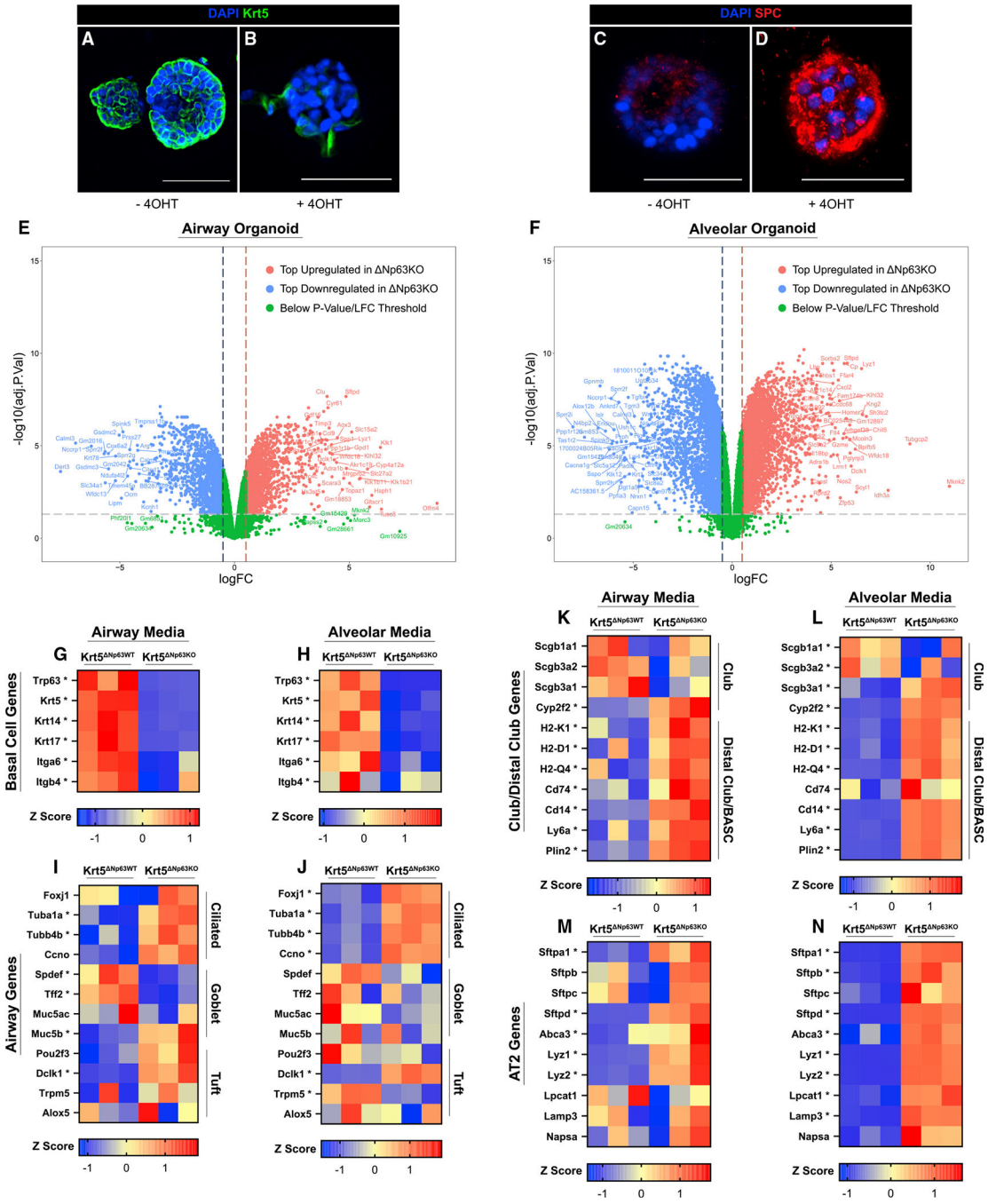

Figure 5. Induced plasticity in ΔNp63^{KO} intrapulmonary p63^{+} progenitors can be directed toward airway or alveolar epithelial fates

(A–D) Representative immunofluorescence images of organoids grown in alveolar medium ± 4OHT. (A and B) The basal cell marker Krt5 is downregulated and disorganized with 4OHT treatment (ΔNp63^{KO}), indicating loss of basal cell identity. (C and D) The AT2 marker SPC is upregulated with 4OHT treatment (ΔNp63^{KO}), indicating acquisition of alveolar fate. Scale bars, 50 μm.

(E and F) Bulk RNA-seq volcano plots of top differentially upregulated and downregulated genes with ΔNp63^{KO} in (E) airway medium and (F) alveolar medium.

(G and H) Basal cell markers are downregulated in both (G) airway and (H) alveolar organoids with $\Delta Np63^{KO}$.

(I and J) Ciliated cell markers are upregulated with $\Delta Np63^{KO}$ in both (I) airway and (J) alveolar organoids. Goblet cell markers are downregulated in airway organoids but unchanged in alveolar organoids with $\Delta Np63^{KO}$ while tuft cell markers are upregulated in airway organoids but unchanged in alveolar organoids with $\Delta Np63^{KO}$.

(K and L) $\Delta Np63^{KO}$ organoids in both media conditions exhibit a shift away from a proximal club identity in favor of a distal club/BASC fate, which becomes more pronounced in alveolar organoids.

(M and N) $\Delta Np63^{KO}$ airway organoids upregulate some AT2 genes while $\Delta Np63^{KO}$ alveolar organoids dramatically upregulate many canonical AT2 markers. Genes marked with an asterisk are statistically significantly differentially expressed with adjusted p value of <0.05.

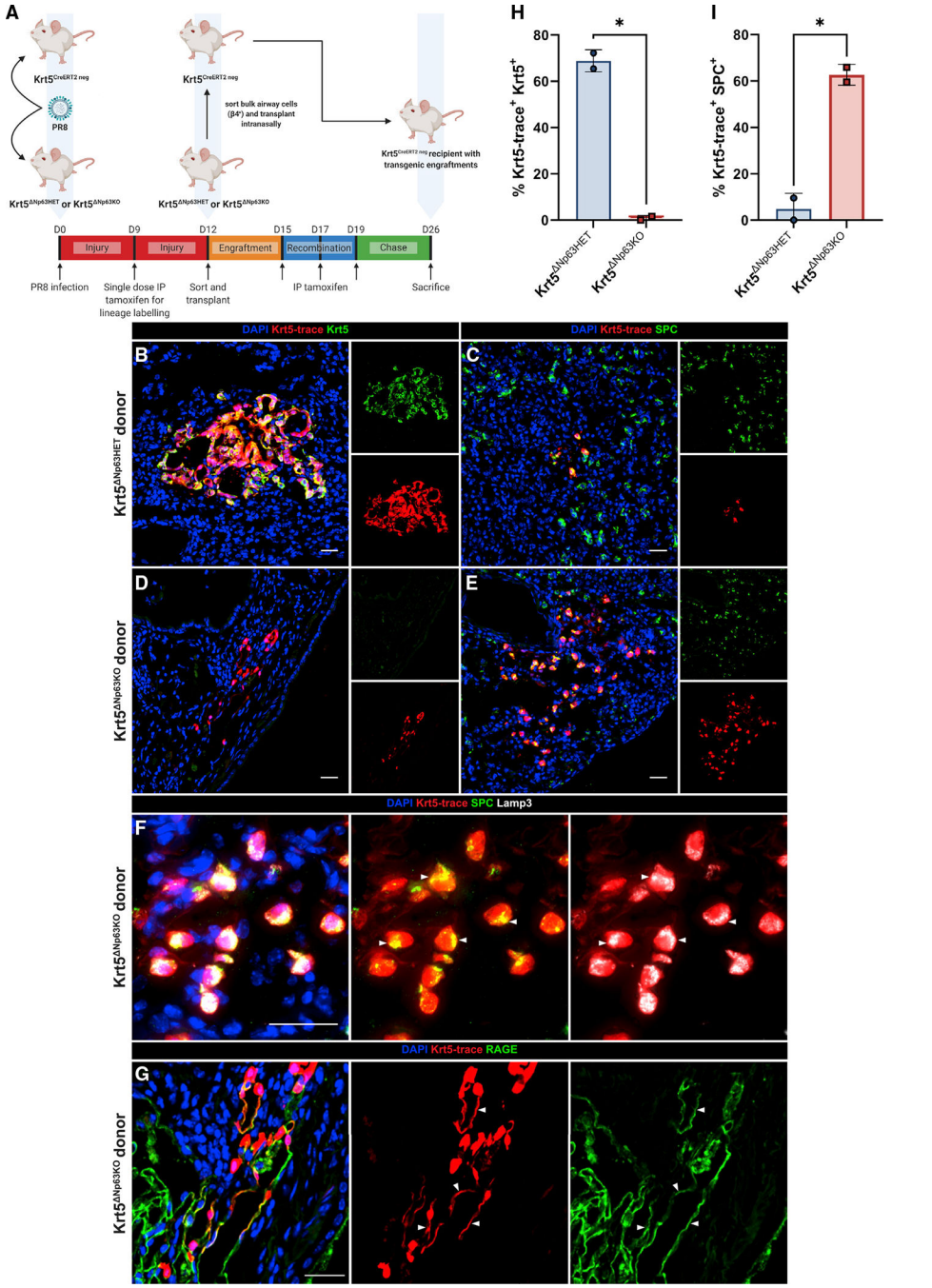

Figure 6. Orthotopic transplantation reveals ΔNp63^{KO} intrapulmonary p63^{+} progenitor-to-AT2 conversion *in vivo*

(A) Schematic of experimental design. Krt5$^{\Delta Np63HET}$ and Krt5$^{\Delta Np63KO}$ donors were infected with PR8 at the same time as Krt5$^{CreERT2\ neg}$ recipients. Three days after a single dose of intraperitoneal (IP) tamoxifen at day 9 post infection to induce lineage labeling in donor cells, EpCAM^{+} β4^{+} airway epithelial cells were sorted from donor mice and transplanted into recipients. Donor cells were allowed to engraft for 3 days, then recipient mice were given three doses of intraperitoneal tamoxifen to induce ΔNp63^{flox} allele recombination. Recipient lungs were harvested 1 week following the final dose of tamoxifen

for engraftment quantification. (B–G) Representative images of engrafted Krt5-trace overlap with lineage markers. $Krt5^{\Delta Np63HET}$ engraftments largely remain as (B) dysplastic Krt5-$trace^{+}$ $Krt5^{+}$ pod-like structures while rare engraftments differentiate into (C) Krt5-$trace^{+}$ SPC^{+} AT2 cells, exhibiting endogenous plasticity. (D) $Krt5^{\Delta Np63KO}$ engraftments lack expression of Krt5, instead generating large regions of (E) Krt5-$trace^{+}$ SPC^{+} AT2s. These $Krt5^{\Delta Np63KO}$ engraftments also express (F) the AT2 marker Lamp3, with white arrows highlighting Krt5-$trace^{+}$ SPC^{+} $Lamp3^{+}$ cells with overlapping SPC and Lamp3 expression, and (G) the AT1 marker RAGE, with white arrows highlighting the overlap of Krt5-$trace^{+}$ cells with RAGE, indicating further differentiation from AT2s into AT1s. Separated channels of indicated immunostains are to the right of each image. Scale bars, 25 μm.

(H) Quantification of Krt5-trace engraftment contribution to $Krt5^{+}$ dysplasia from $Krt5^{\Delta Np63HET}$ and $Krt5^{\Delta Np63KO}$ donors.

(I) Quantification of Krt5-trace engraftment contribution to SPC^{+} AT2s from $Krt5^{\Delta Np63HET}$ and $Krt5^{\Delta Np63KO}$ donors.

Significance based on unpaired Welch's t test. Data presented as mean ± standard deviation with *$p < 0.05$, **$p < 0.01$, ***$p < 0.001$, ****$p < 0.0001$ for all statistics.

KEY RESOURCES TABLE

REAGENT or RESOURCE	SOURCE	IDENTIFIER
Antibodies		
Rabbit anti-SPC	Millipore Sigma	Cat# AB3786; RRID: AB_2755001
rat anti-RAGE	R&D Systems	Cat# MAB1179; RRID: AB_2289349
rabbit anti-Krt5	BioLegend	Cat# 905501; RRID: AB_2565050
chicken anti-Krt5	BioLegend	Cat# 905901; RRID: AB_2565054
goat anti-Scgb3a2	R&D Systems	Cat# AF3465; RRID: AB_2183549
mouse anti-acetylated tubulin	Millipore Sigma	Cat# MABT868; RRID: AB_2819178
rabbit anti-p63α	Cell Signaling	Cat# 13109S; RRID: AB_2637091
rabbit anti-ΔNp63	BioLegend	Cat# 619002; RRID: AB_2207170
rat anti-Ki67	Thermo Fisher Scientific	Cat# 14-5698-82; RRID: AB_10854564
Alexa Fluor™ 488-conjugated donkey anti-rabbit	Thermo Fisher Scientific	Cat# A-21206; RRID: AB_2535792
Alexa Fluor™ 488-conjugated donkey anti-rat	Thermo Fisher Scientific	Cat# A-21208; RRID: AB_2535794
Alexa Fluor™ 488-conjugated donkey anti-goat	Thermo Fisher Scientific	Cat# A-11055; RRID: AB_2534102
Alexa Fluor™ 488-conjugated donkey anti-chicken	Jackson Immunoresearch	Cat# 703-545-155; RRID: AB_2340375
Alexa Fluor™ 488-conjugated donkey anti-mouse	Jackson Immunoresearch	Cat# 715-546-150; RRID: AB_2340849
Alexa Fluor™ 647-conjugated donkey anti-rabbit	Thermo Fisher Scientific	Cat# A-31573; RRID: AB_2536183
Alexa Fluor™ 647-conjugated donkey anti-rat	Thermo Fisher Scientific	Cat# A78947; RRID: AB_2910635
Alexa Fluor™ 647-conjugated donkey anti-goat	Thermo Fisher Scientific	Cat# A-21447; RRID: AB_2535864
Alexa Fluor™ 647-conjugated donkey anti-chicken	Jackson Immunoresearch	Cat# 703-605-155; RRID: AB_2340379
Alexa Fluor™ 647-conjugated donkey anti-mouse	Thermo Fisher Scientific	Cat# A-31571; RRID: AB_162542
FITC-conjugated anti-mouse Ly6D	BioLegend	Cat# 138606; RRID: AB_11203888
rabbit anti-H3K27ac	Cell Signaling	Cat# 8173S; RRID: AB_10949503
rabbit anti-H3K27me3	Cell Signaling	Cat# 9733S; RRID: AB_2616029
rat anti-RAGE	R&D Systems	Cat# MAB1179; RRID: AB_2289349
rabbit anti-Krt5	BioLegend	Cat# 905501; RRID: AB_2565050
chicken anti-Krt5	BioLegend	Cat# 905901; RRID: AB_2565054
goat anti-Scgb3a2	R&D Systems	Cat# AF3465; RRID: AB_2183549
mouse anti-acetylated tubulin	Millipore Sigma	Cat# MABT868; RRID: AB_2819178
rabbit anti-p63α	Cell Signaling	Cat# 13109S; RRID: AB_2637091
rabbit anti-ΔNp63	BioLegend	Cat# 619002; RRID: AB_2207170
rat anti-Ki67	Thermo Fisher Scientific	Cat# 14-5698-82; RRID: AB_10854564
Alexa Fluor™ 488-conjugated donkey anti-rabbit	Thermo Fisher Scientific	Cat# A-21206; RRID: AB_2535792
Alexa Fluor™ 488-conjugated donkey anti-rat	Thermo Fisher Scientific	Cat# A-21208; RRID: AB_2535794
Alexa Fluor™ 488-conjugated donkey anti-goat	Thermo Fisher Scientific	Cat# A-11055; RRID: AB_2534102
Alexa Fluor™ 488-conjugated donkey anti-chicken	Jackson Immunoresearch	Cat# 703-545-155; RRID: AB_2340375
Alexa Fluor™ 488-conjugated donkey anti-mouse	Jackson Immunoresearch	Cat# 715-546-150; RRID: AB_2340849
Alexa Fluor™ 647-conjugated donkey anti-rabbit	Thermo Fisher Scientific	Cat# A-31573; RRID: AB_2536183
Alexa Fluor™ 647-conjugated donkey anti-rat	Thermo Fisher Scientific	Cat# A78947; RRID: AB_2910635

REAGENT or RESOURCE	SOURCE	IDENTIFIER
Alexa Fluor™ 647-conjugated donkey anti-goat	Thermo Fisher Scientific	Cat# A-21447; RRID: AB_2535864
Alexa Fluor™ 647-conjugated donkey anti-chicken	Jackson Immunoresearch	Cat# 703-605-155; RRID: AB_2340379
Alexa Fluor 647-conjugated donkey anti-mouse	Thermo Fisher Scientific	Cat# A-31571; RRID: AB_162542
rabbit anti-H3K27ac	Cell Signaling	Cat# 8173S; RRID: AB_10949503
rabbit anti-H3K27me3	Cell Signaling	Cat# 9733S; RRID: AB_2616029
anti-mouse CD16/31	BioLegend	Cat# 101320; RRID: AB_1574975
APC/Cy7-conjugated rat anti-mouse CD45	BioLegend	Cat# 103116; RRID: AB_312981
Alexa Fluor 488-conjugated rat anti-mouse CD326	BioLegend	Cat# 118210; RRID: AB_1134099
PE/Cy7-conjugated rat anti-mouse CD326	BioLegend	Cat# 118216; RRID: AB_1236471
Alexa Fluor 647-conjugated rat anti-mouse CD104	BioLegend	Cat# 123608; RRID: AB_2563512
Bacterial and virus strains		
PR8	Carolina Lopez Lab (University of Pennsylvania)	N/A
IAV-Cre	Nicolas Heaton Lab (Duke University)	N/A
Biological samples		
Chicken red blood cells	Rockland	Cat# R401-0050
Chemicals, peptides, and recombinant proteins		
PBS	Corning	Cat# MT21-031-CV
HBSS	Thermo Fisher Scientific	Cat# 14175079
DMSO	Millipore Sigma	Cat# D2650
Paraformaldehyde	Thermo Fisher Scientific	Cat# 50-980-495
Normal donkey serum	Millipore Sigma	Cat# D9663
(E/Z)-4-hydroxytamoxifen	Cayman Chemical	Cat# 17308
Tamoxifen	Toronto Research Chemicals	Cat# T006000
Corn oil	Millipore Sigma	Cat# C8267
Triton X-100	Millipore Sigma	Cat# X100
Tween 20	Millipore Sigma	Cat# P1379
BSA	GoldBio	Cat# A-420-100
DAPI	Thermo Fisher Scientific	Cat# D21490
Prolong Gold antifade mountant	Thermo Fisher Scientific	Cat# P36930
Fluoroshield	Millipore Sigma	Cat# F6182
Dispase II	Thermo Fisher Scientific	Cat# 17105041
Penicillin-streptomycin	Thermo Fisher Scientific	Cat# 15140122
Red cell lysis buffer	Millipore Sigma	Cat# A1049201
DNase I	Millipore Sigma	Cat# D4527
Matrigel	Corning	Cat# 354234
Gelatin from bovine skin	Millipore Sigma	Cat# G9391-500G
2.5% trypsin	Thermo Fisher Scientific	Cat# 15090046
EDTA	Thermo Fisher Scientific	Cat# 15575020

REAGENT or RESOURCE	SOURCE	IDENTIFIER
DMEM	Thermo Fisher Scientific	Cat# 11965118
Cosmic calf serum	Thermo Fisher Scientific	Cat# SH3008704
PneumaCult™-Ex Plus Medium	Stemcell Technologies	Cat# 05040
Hydrocortisone	Stemcell Technologies	Cat# 07925
Y-27632 (hydrochloride)	Cayman Chemical	Cat# 10005583
A 83-01	Millipore Sigma	Cat# SML0788
Primocin	Invivogen	Cat# ant-pm-1
IMDM	Thermo Fisher Scientific	Cat# 12440053
Ham's F12	Thermo Fisher Scientific	Cat# 11765047
N2 supplement	Invitrogen	Cat# 17502-048
B27 supplement	Invitrogen	Cat# 15260-037
BSA 7.5% stock	Thermo Fisher Scientific	Cat# 15260037
GlutaMAX	Thermo Fisher Scientific	Cat# 35050-061
8-Bromo-cAMP	Cayman Chemical	Cat# 14431
IBMX	Millipore Sigma	Cat# I5879
1-Thioglycerol	Millipore Sigma	Cat# M6145
Dexamethasone	Millipore Sigma	Cat# D4902
Ascorbic acid	Millipore Sigma	Cat# A4544
CHIR99021	Millipore Sigma	Cat# 252917-06-9
KGF	Peprotech	Cat# 100-19
FGF10	Peprotech	Cat# 100-26
R-spondin1	Peprotech	Cat# 120-38
Noggin	Peprotech	Cat# 250-38
EGF	Peprotech	Cat# AF-100-15
Critical commercial assays		
SimpleChIP Plus Enzymatic Chromatic IP with Magnetic Beads Kit	Cell Signaling	Cat# 9005
NEBNext Ultra II DNA Library Prep Kit for Illumina	NEB	Cat# E7645L
NEBNext Ultra II RNA Library Prep Kit for Illumina	NEB	Cat# E7770L
ReliaPrep RNA Cell Miniprep Kit	Promega	Cat# Z6012
Two-well silicone inserts for migration assay	Ibidi	Cat# 80209
Deposited data		
Loss of ΔNp63 induces epigenetic rewiring and enhances plasticity toward alveolar identity	This paper	GEO: GSE216161
Single-cell RNA-sequencing reveals profibrotic roles of distinct epithelial and mesenchymal lineages in pulmonary fibrosis	John Kropski Lab (Vanderbilt University)	GEO: GSE135893
Longitudinal single-cell transcriptomics analysis of mouse lung upon bleomycin-induced injury	Herbert Schiller Lab (Helmholtz Zentrum München)	GEO: GSE141259
Experimental models: Cell lines		

REAGENT or RESOURCE	SOURCE	IDENTIFIER
MDCK cells	William Beltran Lab (University of Pennsylvania)	N/A
Experimental models: Organisms/strains		
Ai14tdTomato: Gt(ROSA) 26Sor$^{tm14(CAG-tdTomato)Hze}$	Jackson Laboratories	Cat# 007914, RRID: IMSR_JAX:007914
Sox2^{CreERT2}: Sox2$^{tm1(cre/ERT2)Hoch}$	Jackson Laboratories	Cat# 017593, RRID: IMSR_JAX:017593
Krt5^{CreERT2}	Jackson Laboratories	Cat# 029155, RRID: IMSR_JAX:029155
p63^{CreERT2}	Panteleimon Rompolas Lab (University of Pennsylvania)	N/A
ΔNp63^{flox}	Rumela Chakrabarti Lab (University of Pennsylvania)	N/A
Oligonucleotides		
Genotyping primers	See Table S1	N/A
qPCR primers	See Table S2	N/A
Software and algorithms		
Microsoft Excel	Microsoft	https://www.microsoft.com/en-us/microsoft-365/excel
GraphPad Prism 7	GraphPad	https://www.graphpad.com/scientific-software/prism/
Adobe Illustrator	Adobe	https://www.adobe.com/products/illustrator.html
ImageJ	NIH	https://imagej.nih.gov/ij/download.html
LASX	Leica Microsystems	https://www.leica-microsystems.com/products/microscope-software/p/leica-las-x-ls/
R Studio	Posit	https://posit.co/downloads/
Galaxy	The Galaxy Team	https://usegalaxy.org/